Mathematical Modeling of Energy-dense NMC Electrodes: Part II. Data Analysis with Newman Model and with an Extended Model Accounting for Particle Agglomeration

Tuan-Tu Nguyen, Bruno Delobel, Arnaud Demortière, Charles Delacourt

The Electrochemical Society
Advancing solid state & electrochemical science & technology

Mathematical Modeling of Energy-dense NMC Electrodes: Part II. Data Analysis with Newman Model and with an Extended Model Accounting for Particle Agglomeration

Mathematical Modeling of Energy-dense NMC Electrodes: Part II. Data Analysis with Newman Model and with an Extended Model Accounting for Particle Agglomeration

Tuan-Tu Nguyen,[1,2] Bruno Delobel,[2] Arnaud Demortière,[1,3,4] and Charles Delacourt[1,3,z]

[1]*Laboratoire de Réactivité et Chimie des Solides (LRCS), CNRS UMR 7314, Université de Picardie Jules Verne, Hub de l'Energie, Rue Baudelocque, 80039 Amiens Cedex, France*
[2]*Renault Technocentre, 78084 Guyancourt, France*
[3]*Réseau sur le Stockage Electrochimique de l'Energie (RS2E), CNRS FR 3459, Hub de l'Energie, Rue Baudelocque, 80039 Amiens Cedex, France*
[4]*ALISTORE-European Research Institute, CNRS FR 3104, Hub de l'Energie, Rue Baudelocque, 80039 Amiens Cedex, France*

In this second part of this series of papers, the use of two physics-based models to analyze the discharge performance of a set of high-energy-density electrodes is discussed. The measured set of parameters from the first part is implemented into these models. First, the regular Newman pseudo-2D model shows a large discrepancy against the experimental values. Then, an extension of the Newman model considering the particle agglomeration due to the calendering effects is presented, allowing for the validation of discharge rate capabilities of all studied industry-grade electrodes with different electrolytes. At the agglomerate scale, the model accounts for both the ionic transport in sub-pores and the inter-particle solid diffusion. The simulation results from this work demonstrate that increasing the electrode loading and/or density leads to either a higher fraction of sub-pores (at the expense of that of macropores) or larger porous agglomerate size, resulting in a poor rate performance. The model analysis suggests that a substantial gain in performance at high C-rates is expected if agglomeration effects are mitigated in these high-energy electrodes.
© 2022 The Author(s). Published on behalf of The Electrochemical Society by IOP Publishing Limited. This is an open access article distributed under the terms of the Creative Commons Attribution 4.0 License (CC BY, http://creativecommons.org/licenses/by/4.0/), which permits unrestricted reuse of the work in any medium, provided the original work is properly cited. [DOI: 10.1149/1945-7111/ac72c8]

List of symbols

A_{PA}	m^2_{PA}/m^3_{PE}	specific interfacial area between the PA and the liquid phase in macro-pore domain per unit volume of PE
a_{AM-3}	m^2_{AM-3}/m^3_{PA}	specific interfacial area between the AM and the liquid phase in the sub-pore domain at PA scale
a_{AM-AM}	m^2_{AM-AM}/m^3_{PA}	specific interfacial area between the AM particles at PA scale
$\bar{c}_s$	mol/m^3_{AM}	local volume-averaged solid Li concentration of AM phase within the PA
$c_{s, surf}$	mol/m^3_{AM}	concentration at the surface of the AM particle
$c_{s, max}$	mol/m^3_{AM}	maximum concentration of intercalated Li in AM particle
c_s	mol/m^3_{AM}	solid-phase Li concentration within the AM particle
$c_{3,0}$	mol/m^3	solvent concentration in a binary electrolyte filled in sub-pores
c_3	mol/m^3	salt concentration in a binary electrolyte filled in sub-pores
$C_{2,0}$	mol/m^3	solvent concentration in a binary electrolyte filled in macro-pores
C_2	mol/m^3	salt concentration in a binary electrolyte filled in macro-pores
d_{50}	μm	median diameter of AM particles
D	m^2/s	bulk diffusion coefficient of the liquid phase
$D_{eff, i}$	m^2/s	effective salt diffusion coefficient of the liquid phase in phase i
D_s	m^2/s	diffusion coefficient of Li in the AM particles
F	C/mol	Faraday's constant
f_{AM-3}		fraction of particle surface in contact with the electrolyte in sub-pores
$\vec{I}_1$	A/m^2_{CC}	electronic current density across the PE in the solid phase
$\vec{I}_2$	A/m^2_{CC}	ionic current density across the PE in the liquid phase
$\vec{i}_i$	A/m^2_{CC}	ionic current density in liquid phase in phase i at PA scale
i		used as a subscript indicating a coexisting phase presented in the PE
i_n^0	A/m^2_{ASA}	exchange current density
i_{Li}^0	$A/m^2_{Li foil}$	exchange current density at the Li foil
I	A	applied current in the μ4-probe experiment
I_{app}	A/m^2_{CC}	discharge current density

[z]E-mail: charles.delacourt@u-picardie.fr

(Continued).

$j_{\text{int},+}$	$\text{mol}/(\text{m}^2_{\text{AM}-3}\cdot\text{s})$	cation internal pore-wall flux
$j_{3,-}$	$\text{mol}/(\text{m}^2_{\text{PA}}\cdot\text{s})$	anion flux reciprocally flowing between macro-pore domain in PE and sub-pore domain within PA
$j_{3,+}$	$\text{mol}/(\text{m}^2_{\text{PA}}\cdot\text{(HTML translation failed)}\text{s})$	cation flux reciprocally flowing between macro-pore domain in PE and sub-pore domain within PA
$j_{\text{AM}-\text{AM}}$	$\text{mol}/(\text{m}^2_{\text{AM}-\text{AM}}\cdot\text{s})$	rate of transfer of solid Li from the active secondary particle to another active secondary particle
j_{total}	$\text{mol}/(\text{m}^2_{\text{AM}}\cdot\text{s})$	total flux entering the AM particle
k_0	$\text{mol}/[\text{m}^2_{\text{ASA}}\cdot\text{s}\cdot(\text{mol}/\text{m}^3)^{1.5}]$	reaction rate constant of the AM
$k_{0,\text{Li}}$	$\text{mol}/[\text{m}^2_{\text{Li foil}}\cdot\text{s}\cdot(\text{mol}/\text{m}^3)^{0.5}]$	reaction rate constant of Li foil
L_{el}	μm	PE thickness
L_{sep}	μm	separator thickness
$\vec{n}$		unit vector normal to a plane
$\vec{N}_{2,-}$	$\text{mol}/(\text{m}^2_{\text{CC}}\cdot\text{s})$	flux density of the anion in macro-pore domain at PE scale
$\vec{n}_{3,-}$	$\text{mol}/(\text{m}^2_{\text{PA}}\cdot\text{s})$	flux density of the anion in sub-pore domain at PA scale
$\vec{n}_{\text{AM}-\text{AM}}$	$\text{mol}/(\text{m}^2_{\text{AM}-\text{AM}}\cdot\text{s})$	Li flux diffusing between AM particles within the PA
$\vec{n}_s$	$\text{mol}/(\text{m}^2_{\text{AM}}\cdot\text{s})$	Li flux in the AM particle
Q_{th}	Ah/kg	Electrode Theoretical Capacity
$\bar{q}$	$\text{mol}/(\text{m}^3_{\text{AM}}\cdot\text{s})$	volume-average concentration flux
R	J/(mol·K)	ideal gas constant
R	Ω	sample resistance determined by the μ4-probe experiment
R_{PA}	μm	PA radius
r	μm	radial dimension along the AM particle
r^*		radial dimension of the PA
r_{P}	μm	radius of a NMC secondary particle
T	K	absolute temperature
$T_{\text{elyte, 3}}$	s	characteristic time of ionic transport in electrolyte in sub-pores of the PA
t	s	time
t_+^0		transference number of Li^+ in the electrolyte with respect to the solvent velocity
U	V	equilibrium potential of the AM
ΔV	V	voltage drop between the two inner contacts in the μ4-probe experiment
$\vec{v}_0$	m/s	the solvent velocity
x	μm	dimension across the sandwich
x_0		initial stoichiometry
Greek Symbols		
α		thermodynamic factor
β		charge transfer coefficient
ε_{sep}	$\text{m}^3_{\text{elyte}}/\text{m}^3_{\text{sep}}$	separator porosity
ε_i	$\text{m}^3_i/\text{m}^3_{\text{PA}}$	volume fraction of phase i at PA scale
κ	S/m	bulk ionic conductivity of the electrolyte
$\kappa_{\text{eff},i}$	S/m	effective ionic conductivity of the liquid phase in phase i
ρ_{el}	g/cm^3	electrode density
σ_{eff}	S/m	effective electronic conductivity of the solid phase of the electrode
τ_{AM}		tortuosity factor of the AM phase
τ_{Br}		tortuosity factor of the liquid phase by Bruggeman
$\tau_{\text{e},i}$		electrode tortuosity factor of phase i at PA scale
τ_{e}		electrode tortuosity factor
τ_{sep}		separator tortuosity factor
ξ_3		ratio of sub-pore domain among the total porosity of the PE
$\Phi_{1,\text{Li}}$	V	electric potential at Li foil
Φ_i	V	electric potential of phase i
Ψ	$\text{m}^3_{2+3}/\text{m}^3_{\text{PE}}$	total porosity of the PE
Ψ_i	$\text{m}^3_i/\text{m}^3_{\text{PE}}$	volume fraction of phase i at PE scale
Ψ_{PA}	$\text{m}^3_{\text{PA}}/\text{m}^3_{\text{PE}}$	PA volume fraction at PE scale

Due to the complexity of the underlying physics involving during the operation of Li-ion battery (LiB), an experimental approach by itself can be not sufficient to achieve a full understanding of the cell behavior. Physics-based models of the LiB demonstrate the great capacity to provide valuable insights, as they can decipher and quantify the electrode limitations. A reliable model also allows exploring different scenarios at a limited cost and time compared to a full experimental approach. The improvement of the electrode performance through its microstructure design can, therefore, be accelerated.

In light of this, many works focus on building numerical models for LiNi$_x$Mn$_y$Co$_{(1-x-y)}$O$_2$ (NMC) electrodes since the NMC is a popular class of material for the cathode. Despite the high extent of the investigation, the interplay between the electrode performance and its microstructure has not been completely unveiled. Several works reported that the somewhat mediocre performance of high-energy-density NMC electrodes at high C-rates relates to the transport limitation in electrolyte-filled pores. Therefore, the tortuosity of the pore network is assigned to be the main rate-limiting factor.

In contrast, Appiah et al.[1] and Xu et al.[2] validated their models by investigating the solid diffusion within the active secondary particles, for which an empirical relationship of the solid diffusion coefficient with the electrode thickness and the C-rate was set forth. Although these correlations allow for a good agreement between simulations and experimental results, the approach relies on fitted correlations rather than on a physical foundation.

In the first part of this series of papers, a combined experimental/modeling approach relying on the Newman pseudo-2D (P2D) model[3–5] for a complete electrode characterization was presented. Intrinsic properties of the LiNi$_5$Mn$_3$Co$_2$O$_2$ were determined and validated using thin electrodes having negligible porous-electrode effects. The validation on the discharge rate capability of a lab-made low loading electrode provided a trustworthy set of parameters for the active material in Newman P2D model. For electrode-related properties, industry-grade electrodes were characterized using appropriate experimental methods, which are widely reported in the literature. As the parameters determined in part I look consistent, the aim of this second part is to simulate the performance of these industry-grade electrodes and assess to which extent simulations and experimental data agree with each other. The popular Newman battery model is selected to this end. In case simulations significantly depart from experimental data, a refined physical representation is adopted. Toward this goal, an extension of Newman model is developed and discussed in this work, which considers the formation of porous agglomerates within industry-grade electrodes due to the calendering effects when reaching a high density. Within a porous agglomerate, a sub-pore domain exists and inter-connectivity between particles is likely to occur, which differs from the configuration at the particle scale in the regular Newman P2D model. Additional limitations due to the porous agglomerates (PA) formation can, therefore, be considered with our proposed model. Later, we demonstrate that this model allows good agreement with the experimental results, while the regular Newman model tends to overestimate the electrode performance.

All the parameters obtained in the first paper serve as input parameters of the two models in this work for the validation of the discharge rate capabilities of the industry-grade electrodes. After validation, the performance of different electrode designs is analyzed using the model, i.e., the electrode overpotential is decorrelated into each polarization source for a low- and a high-loading electrode design. Results obtained from this model-based analysis are eventually discussed. Finally, as a perspective for optimizing high-energy-density electrode design, the performance benefits if agglomerate formation is suppressed are examined with the model.

Model Theory

In this paper, since lithium metal is used in place of a porous negative electrode, a half cell is modeled. The model consists of one NMC electrode and one separator domains, whereas only the outer surface of the Li foil and the current collector (CC) are represented through their boundary with the separator and the electrode, respectively, for the sake of simplicity. Also, it is assumed that the volume variation of NMC particles is negligible during the Li (de)insertion process. As a result, the geometry of the pore domain remains unchanged throughout the battery operation.

Porous agglomerate model.—Newman half-cell model is extended to consider the particle agglomeration that is prone to occur because of the calendering process. Particle agglomerates consist of individual NMC secondary particles densely packed together with CBD and pores. The pores located in these PAs are assumed to be very small and narrow due to the high density of the solid mixture, so that they are denoted as sub-pores. Since the NMC secondary particle diameter is more than thirty times that of the primary particles, the primary particles are not considered explicitly, along with grain-boundary effects that might exist. Instead, the agglomerates that we refer to here result from the agglomeration of secondary particles.

Thus, we introduce herein an extension of Newman model that takes into account the presence of such PAs instead of individual AM particles. The model's mathematical methodology relies on the porous electrode theory in the same manner as the Newman model. Likewise, the electrolyte transport in the electrolyte phase of the electrode is described by concentrated solution theory. The model is implemented and solved with COMSOL Multiphysics.

Regarding the PA model, Dargaville et al.[6] proposed a 1D + 1D + 1D (P3D) model for modeling the LiFePO$_4$ electrode. The three corresponding scales are namely the porous electrode (PE), the PA, and the LiFePO$_4$ particles located inside the PA. Based on this work, several follow-up works[7–9] developed models for electrodes having an agglomerate structure of the AM particles (e.g. NMC, Li(Ni$_{1/3}$Co$_{1/3}$Al$_{1/3}$)O$_2$) with an inner pore structure. Nevertheless, these works used the PA model to consider the morphology of individual secondary particles, which differs from the concept in this paper.

Purposely, the model in this work is kept as simple as possible to minimize the number of additional parameters with respect to the regular Newman P2D model. It is decided to resort to the polynomial approximation to treat the solid diffusion in NMC particles, as proposed by Subramanian et al.[10] They developed efficient approximate solutions for the solid diffusion within AM secondary particles by assuming that the Li concentration inside the spherical particle can be expressed as a polynomial across the radial dimension. Therefore, solid diffusion within AM particles is solved by a set of ordinary differential equations and algebraic equations.

In Ref. 10, the authors demonstrated that the approximate model using high order (4th-order) polynomial to represent the Li concentration profile within the particles yields a great extent of accuracy that is tantamount to the Newman P2D model. The polynomial is, then, solved in terms of volume-average AM-phase Li concentration, particle surface concentration and volume-average concentration flux.

Since a variable solid diffusion coefficient is considered here instead of a constant coefficient as in Ref. 10, it is taken to be a function of the volume-average Li concentration instead of the local Li concentration in the P2D model. The error of this assumption on the simulations is investigated later when comparing the simulated rate capability upon discharge using Newman model with polynomial approximation against that from the Newman P2D model for the same electrode (see Fig. S1 (available online at stacks.iop.org/JES/169/060510/mmedia)). The solid diffusion coefficient has been adapted in part I of this series of papers to take into account this discrepancy between the two models.

A schematic diagram of the model is illustrated in Fig. 1. The "macro model" refers to the PE scale just like in the Newman P2D model. At the PE scale, there is a liquid phase filling in the macro-pore domain and a solid phase, which is made up of PA (referred to as "micro model"). These agglomerates contain the AM, the CBD and a sub-pore domain filled with electrolyte. It is worth noting that by representing in this way, the AM particles are no longer assumed to be isolated and fully exposed to the liquid phase like in the regular Newman model, as it does not seem to hold true anymore for high-density electrodes. The total electrode porosity is the sum of the porosities in both sub-pore and macro-pore domains.

The PA is assumed to be spherical and radially symmetric. In addition, the interface between secondary particles located at the outer of the PA and electrolyte in macro-pores (i.e., the outer surface of the agglomerate) is assumed to be inactive, i.e., there is no charge
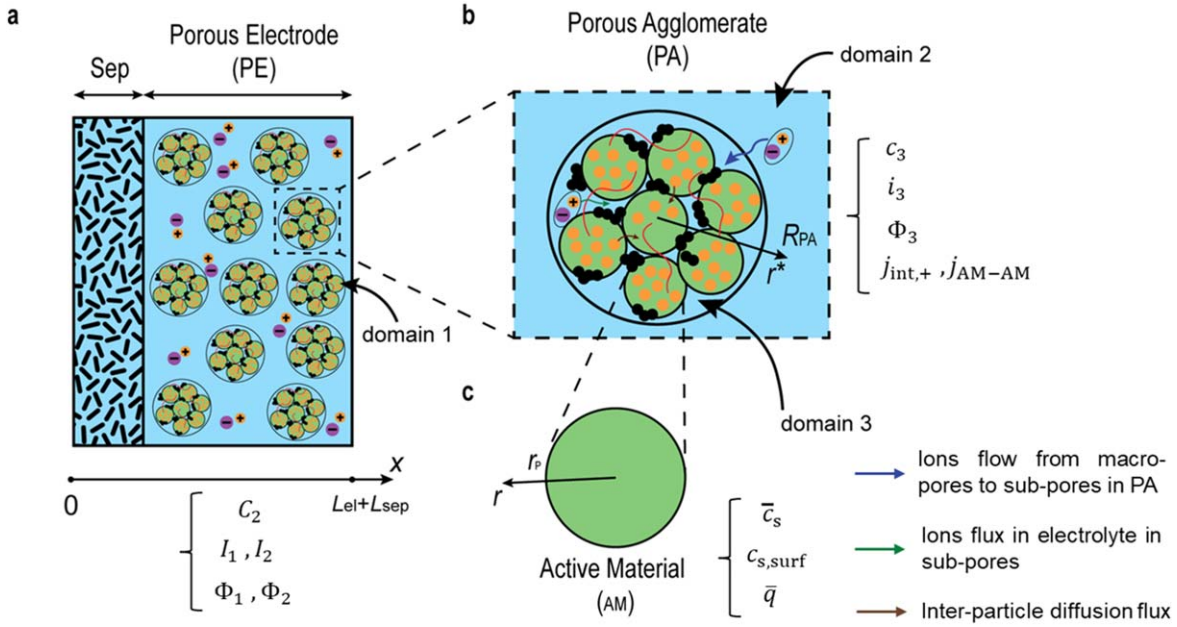
Figure 1. Schematic of our proposed model (1D + 1D + 1D) having polynomial approximation for particle scale. Two size scales are presented in (a) and (b) for Porous Electrode and Porous Agglomerate, respectively. (c) The polynomial approximation is adopted for the solid diffusion within the active secondary particles.

transfer process at the PA/macro-pores interface. Thus, the pore-wall flux occurs only at the interface between AM and sub-pores located inside the PA.

Within the PA, AM particles are considered spherical with a uniform diameter. It is worth noting that the PA can be extremely dense, which promotes an inter-connectivity between solid particles. Consequently, unlike in the Newman model, the AM particle surface are not completely exposed to the electrolyte such that the active surface area is decreased compared to the value in Newman model. Although the particle/particle interface is not active for electrochemical reaction, it is assumed to allow for an inter-particle Li diffusive flux, the rate of which depends on the difference in surface concentrations of adjacent particles. As a result, a mass balance of inserted Li in AM phase via different paths at PA scale is introduced into the model.

Finally, it is worth mentioning that the effective electronic conductivity of the solid phase in the "macro model," i.e. across the electrode thickness, is assumed to be constant. This might not be valid if the conductive pathway is a mixture of CBD and NMC, since the electronic conductivity of the NMC materials has been reported to vary as a function of the Li content.[11] Besides, within the PA, the CB network is assumed to be well percolated, so that there is no limitation from electronic transport. Thus, the electric potential is uniformly distributed throughout the PA, i.e., there is no ohmic drop in the solid phase across the radial dimension of the PA. The assumption of no electronic transport limitations within the PA might break down at a high discharge C-rate. In that case, governing equations for electronic transport across the PA could be readily added to the actual model.

For the sake of understanding, at the PE scale ("macro model"), the solid phase that consists of AM and CBD is referred to as domain 1, the liquid phase is referred to domain 2, whereas at the PA scale ("micro model"), the liquid phase in the sub-pore domain is referred to as domain 3. The AM phase within the PA is subscripted with $_{AM}$. The parameters pertaining to the PE scale (domains 1 and 2) are denoted with uppercase symbols, whereas lowercase symbols are dedicated to parameters pertaining to the PA scale (domain 3 and $_{AM}$). The model is also referred to as the PApa model, which comes from **P**orous **A**gglomerate and **p**olynomial **a**pproximation for solid diffusion in the active secondary particles.

"Macro model".—Regarding the "macro model," an electronic current density $\vec{I}_1$ flows across the PE in the solid phase along the x dimension (i.e., across the electrode thickness), and an ionic current density $\vec{I}_2$ flows similarly in the liquid phase. The sum of these two current densities is uniform across the PE, which means that any increase in $\vec{I}_2$ is compensated for by a decrease in $\vec{I}_1$. For the macroscopic model, this is expressed as:

$$\nabla \cdot \vec{I}_1 + \nabla \cdot \vec{I}_2 = 0 \qquad [E1]$$

By electroneutrality in the solution, a current balance relates the divergence of the ionic current density to the net cation flux leaving the macro-pore domain to enter the sub-pore domain:

$$\nabla \cdot \vec{I}_2 = A_{PA} F (j_{3,+} - j_{3,-}) \qquad [E2]$$

in which A_{PA} (m_{PA}^2/m_{PE}^3) is the specific interfacial area between the PA and the liquid phase in macro-pore domain per unit volume of PE and F is the Faraday's constant. Given a spherical shape of the PA having a radius, R_{PA}, it is common in a macro-homogenous model that A_{PA} is estimated from the PA volume fraction, $\Psi_{PA}(m_{PA}^3/m_{PE}^3)$, using the following equation:

$$A_{PA} = \frac{3\Psi_{PA}}{R_{PA}} \qquad [E3]$$

The net cation flux $j_{3,+} - j_{3,-}$ ($mol/m_{PA}^2 \cdot s$) relates to the amount of Li$^+$ consumed/produced by the electrochemical reactions occurring within the PA, at the interface between the AM particles and the sub-pores.

From E1, the electronic current balance in the solid phase is inferred:

$$\nabla \cdot \vec{I}_1 = -A_{PA} F (j_{3,+} - j_{3,-}) \qquad [E4]$$

The electronic current density in solid phase $\vec{I}_1$ is simply described with Ohm's law, with Φ_1 the electric potential of the solid phase and σ_{eff} the effective electronic conductivity of the solid phase of the electrode.

$$\vec{I}_1 = -\sigma_{\text{eff}} \nabla \Phi_1 \qquad [E5]$$

The ionic current density in liquid phase $\vec{I}_2$ is expressed using the Mac-Innes equation that derives from the concentrated solution theory and accounts for salt concentration gradients across the liquid phase in addition to potential gradients.

$$\vec{I}_2 = -\kappa_{\text{eff},2} \nabla \Phi_2 + 2\kappa_{2,\text{eff}} \frac{RT}{F}(1 - t_+^0)\alpha \nabla \ln C_2 \qquad [E6]$$

In this equation, R is the ideal gas constant, T is the absolute temperature, t_+^0 is the transference number of Li^+ in the electrolyte with respect to the solvent velocity, α is the thermodynamic factor, and $\kappa_{\text{eff},2}$ stands for the effective ionic conductivity of the electrolyte within the macro-pore domain. The effective ionic conductivity can be calculated from the bulk ionic conductivity κ by:

$$\kappa_{\text{eff},2} = \frac{\Psi_2}{\tau_{\text{e},2}}\kappa \qquad [E7]$$

where $\Psi_2 (\text{m}_2^3/\text{m}_{\text{PE}}^3) = 1 - \Psi_{\text{PA}}$ is the volume fraction of the macro-pore domain, and $\tau_{\text{e},2}$ is the electrode tortuosity factor of the macro-pore domain.

It is noteworthy that E6 is strictly valid for a binary electrolyte, i.e., a salt and a single solvent mixture. Newman and coworkers consider that solvent components commonly used in LiB are similar enough to be approximated as a single solvent component.[12]

In the separator domain, the charge is conserved, hence E2 reduces to:

$$\nabla \cdot \vec{I}_2 = 0 \qquad [E8]$$

The ionic current density is continuous at the interface between separator and the PE.

Since only potential differences, and not absolute potentials, are measurable, Φ_2 has an arbitrary datum as a boundary condition. Here, we set the reference potential at the PE/CC boundary:

$$\Phi_2 = 0 \qquad [BC1]$$

At the Li foil, a boundary condition specifies all the applied current is carried by the ionic current in the liquid phase:

$$\vec{I}_2 \cdot \vec{n} = Fi_{\text{Li}}^0 \left\{ \exp\left(\frac{(1-\beta)F}{RT}(\Phi_{1,\text{Li}} - \Phi_2)\right) \right.$$
$$\left. - \exp\left(-\frac{\beta F}{RT}(\Phi_{1,\text{Li}} - \Phi_2)\right) \right\} = -I_{\text{app}} \qquad [BC2]$$

where, $i_{\text{Li}}^0 = Fk_{0,\text{Li}}C_2^{1-\beta}$ represents the exchange current density at the Li foil, where the reaction $Li \leftrightarrow Li^+ + e^-$ occurs, I_{app} represents the discharge current density (A/m_{CC}^2), which is negative for Li insertion in AM phase by convention.

At the PE/CC boundary, the ionic current is set to be 0, as all applied current is carried by the electronic current in the solid phase:

$$\vec{I}_2 \cdot \vec{n} = 0 \qquad [BC3]$$

For the solid phase, the electronic current density is assumed to be equal to the applied current density at the CC:

$$\vec{I}_1 \cdot \vec{n} = I_{\text{app}} \qquad [BC4]$$

At separator/PE boundary, the electronic current density is set to be 0, as the total current is carried by ions only:

$$\vec{I}_1 \cdot \vec{n} = 0 \qquad [BC5]$$

From porous electrode theory, the mass balance for the anion across the PE reads:

$$\Psi_2 \frac{\partial C_2}{\partial t} = -\nabla \cdot \vec{N}_{2,-} + A_{\text{PA}} j_{3,-} \qquad [E9]$$

where $A_{\text{PA}} j_{3,-}$ is the anion flux per unit volume of PE, that reciprocally flows between macro-pore domain in PE and sub-pore domain in PA.

The flux density of the anion is described by concentrated solution theory as:

$$\vec{N}_{2,-} = -\left(1 - \frac{d \ln C_{2,0}}{d \ln C_2}\right)D_{\text{eff},2} \nabla C_2 - (1 - t_+^0)\frac{\vec{I}_2}{F} + C_2 \vec{v}_0 \quad [E10]$$

where $C_{2,0}$ is the solvent concentration, $\vec{v}_0$ is the solvent velocity, and $D_{\text{eff},2}$ represents the effective salt diffusion coefficient in the macro-pore domain.

Similar to the effective conductivity, the effective salt diffusion coefficient can be calculated from the bulk salt diffusion coefficient D by:

$$D_{\text{eff},2} = \frac{\Psi_2}{\tau_{\text{e},2}}D \qquad [E11]$$

It is common in papers relying on Newman model that the convection term $c_2 \vec{v}_0$ in the anion flux expression is ignored, assuming that convection is negligible. Likewise, one generally assumes the term $\frac{d \ln C_{2,0}}{d \ln C_2}$ to be zero.

The flux density of the anion is zero at the PE/CC boundary; and at the Li foil surface, where all the current is carried by ionic (Li^+) current:

$$\vec{N}_{2,-} \cdot \vec{n} = 0 \text{ at } x = 0 \qquad [BC6]$$

and

$$x = L_{\text{el}} + L_{\text{sep}} \qquad [BC7]$$

The concentration and flux are continuous at the boundary between the separator and the porous electrode.

"Micro model".—The volume fraction of the sub-pore domain, $\Psi_3 (\text{m}_3^3/\text{m}_{\text{PE}}^3)$ is expressed as:

$$\Psi_3 = \Psi - \Psi_2 = \xi_3 \Psi \qquad [E12]$$

where ξ_3 is the ratio of sub-pore domain among the total porosity of the PE, $\Psi (\text{m}_{2+3}^3/\text{m}_{\text{PE}}^3)$.

From E12, we can infer the volume fraction of the sub-pore domain at PA scale, $\varepsilon_3 (\text{m}_3^3/\text{m}_{\text{PA}}^3)$, by:

$$\varepsilon_3 = \frac{\Psi_3}{\Psi_{\text{PA}}} \qquad [E13]$$

The mass transport in the electrolyte filling in the sub-pore domain is also described by concentrated solution theory. For the sake of simplicity, the mass balance for the anion is considered:

$$\varepsilon_3 \frac{\partial c_3}{\partial t} = -\nabla \cdot \vec{n}_{3,-} \qquad [E14]$$

where:

$$\vec{n}_{3,-} = -\left(1 - \frac{d \ln c_{3,0}}{d \ln c_3}\right)D_{\text{eff},3} \vec{\nabla} c_3 - (1 - t_+^0)\frac{\vec{i}_3}{F} \approx$$
$$-D_{\text{eff},3} \vec{\nabla} c_3 - (1 - t_+^0)\frac{\vec{i}_3}{F} \qquad [E15]$$

where $D_{\text{eff},3} = \frac{\varepsilon_3}{\tau_{\text{e},3}} D$ represents the effective salt diffusion coefficient in the sub-pore domain. The electrode tortuosity factor of the sub-pores is $\tau_{\text{e},3}$. $c_{3,0}$ is the solvent concentration. Similar to the macro-pore domain, the convection term $c_3 \vec{v}_0$ in the anion flux expression is also ignored and $\frac{d \ln c_{3,0}}{d \ln c_3}$ is assumed to be zero.

The flux density of anion is zero at the PA center by symmetry. At the PA surface, one has the continuity of the salt concentration between the sub-pore and macro-pore domains. As the result, we get:

$$\vec{n}_{3,-} \cdot \vec{r^*} = 0 \text{ at } r^* = 0 \qquad [\text{BC8}]$$

$$c_3 = C_2 \text{ at } r^* = R_{\text{PA}} \qquad [\text{BC9}]$$

Moreover, the continuity of the anion and cation fluxes at the PA surface holds:

$$\vec{n}_{3,-} \cdot \vec{r^*} = -D_{\text{eff},3} \frac{\partial c_3}{\partial r^*} - (1 - t_+^0) \frac{i_{3,r^*}}{F} = j_{3,-} \qquad [\text{E16}]$$

$$\vec{n}_{3,+} \cdot \vec{r^*} = -D_{\text{eff},3} \frac{\partial c_3}{\partial r^*} + t_+^0 \frac{i_{3,r^*}}{F} = j_{3,+} \qquad [\text{E17}]$$

These two extra equations are both required to solve for the cation and anion fluxes, which are not equal to each other at the macro-pore/sub-pore boundary. It is worth mentioning that at any time, the cation flux entering the sub-pore domain from the macro-pore domain corresponds to that of the anion plus the overall Li flux inserting into the solid particles of the porous agglomerate.

The current balance in electrolyte filling in the sub-pore domain reads:

$$\nabla \cdot \vec{i}_3 = a_{\text{AM}-3} F j_{\text{int},+} \qquad [\text{E18}]$$

where $a_{\text{AM}-3}(\text{m}^2_{\text{AM}-3}/\text{m}^3_{\text{PA}})$ the specific interfacial area between the AM and the liquid phase in the sub-pore domain and $j_{\text{int},+}$ the cation internal pore-wall flux. The internal pore-wall flux $j_{\text{int},+}$ corresponds to the rate of the electrochemical reaction for Li$^+$ insertion/deinsertion and is detailed in the following.

Since the particle surface is likely not fully exposed to the electrolyte in sub-pores due to the inter-connectivity between solid particles, we introduce a new variable, $f_{\text{AM}-3}$ representing the fraction of particle surface in contact with the electrolyte in sub-pore domain. Therefore, $a_{\text{AM}-3}$ is estimated using the following equation:

$$a_{\text{AM}-3} = \frac{3 \varepsilon_{\text{AM}} f_{\text{AM}-3}}{r_{\text{P}}} \qquad [\text{E19}]$$

where $\varepsilon_{\text{AM}}(\text{m}^3_{\text{AM}}/\text{m}^3_{\text{PA}}) = 1 - \varepsilon_3 - \varepsilon_{\text{CBD}}$ is the volume fraction of AM phase at PA scale, with $\varepsilon_{\text{CBD}}(\text{m}^3_{\text{CBD}}/\text{m}^3_{\text{PA}})$ is the volume fraction of CBD at PA scale, and r_{P} is the radius of NMC secondary particles.

The ionic current density in liquid phase $\vec{i}_3$ is expressed by means of Mac-Innes equation, according to:

$$\vec{i}_3 = -\kappa_{\text{eff},3} \nabla \Phi_3 + 2\kappa_{\text{eff},3} \frac{RT}{F}(1 - t_+^0) \alpha \nabla \ln c_3 \qquad [\text{E20}]$$

where $\kappa_{\text{eff},3} = \frac{\varepsilon_3}{\tau_{\text{e},3}} \kappa$ stands for the effective ionic conductivity of the electrolyte within the sub-pore domain.

Two boundary conditions are required for solving for Φ_3 by combining E18 and E20. The ionic current density is equal to zero at the PA center by symmetry. At the PA surface, there is a continuity of the liquid-phase potential between sub-pore and macro-pore domains.

$$\vec{i}_3 \cdot \vec{r^*} = 0 \text{ at } r^* = 0 \qquad [\text{BC10}]$$

$$\Phi_3 = \Phi_2 \text{ at } r^* = R_{\text{PA}} \qquad [\text{BC11}]$$

At the PA scale, an additional mass balance applied to inserted "neutral" Li in the AM phase is introduced, which considers the inter-particle solid diffusion through the AM/AM interface. It is an additional pathway for Li transport across the radial dimension of the PA, alongside with the Li$^+$ transport across the sub-pores followed by electrochemical insertion in the AM. Based on the porous electrode theory applied to the active-material phase of the PA scale, it reads:

$$\varepsilon_{\text{AM}} \frac{d\bar{c}_{\text{s}}}{dt} = -\nabla \cdot \vec{n}_{\text{AM}-\text{AM}} - a_{\text{AM}-3} j_{\text{int},+} \qquad [\text{E21}]$$

With $\bar{c}_{\text{s}}$ is the local volume-averaged solid Li concentration of AM phase within the PA; $\vec{n}_{\text{AM}-\text{AM}} = -\frac{\varepsilon_{\text{AM}}}{\tau_{\text{AM}}} D_{\text{s}} \vec{\nabla} \bar{c}_{\text{s}}$ represents the Li flux diffusing between AM particles within the PA; τ_{AM} is the tortuosity factor of the AM phase.

At particle scale, the transport model is based on solid diffusion of "neutral" Li species, and reads:

$$\frac{dc_{\text{s}}}{dt} = -\nabla \cdot \vec{n}_{\text{s}} \qquad [\text{E22}]$$

with $\vec{n}_{\text{s}}$ the Li flux in the AM particle, which is zero at the particle center (by symmetry) and which is set equal to the total flux, $j_{\text{total}} (\text{mol}/(\text{m}^2_{\text{AM}} \cdot \text{s}))$ entering the particle at the surface.

$$\vec{n}_{\text{s}} \cdot \vec{r} = 0 \text{ at } r = 0 \qquad [\text{BC12}]$$

$$\vec{n}_{\text{s}} \cdot \vec{r} = j_{\text{total}} \text{ at } r = r_{\text{P}} \qquad [\text{BC13}]$$

The total flux entering the AM particle is set equal to the sum of the two contributions at the particle surface, which gives:

$$j_{\text{total}} = f_{\text{AM}-3} j_{\text{int},+} + (1 - f_{\text{AM}-3}) j_{\text{AM}-\text{AM}} \qquad [\text{E23}]$$

where, $j_{\text{AM}-\text{AM}} (\text{mol}/(\text{m}^2_{\text{AM}-\text{AM}} \cdot \text{s}))$ is the rate of transfer of solid Li from the AM particle to another AM particle, and $(1 - f_{\text{AM}-3})$ is the fraction of AM particle surface in contact with other AM particles (fraction covered with CBD is assumed to be negligible here).

To resolve the transport model at particle scale, the polynomial approximation is adopted, so that the particle dimension is dropped. The detail of the development of the polynomial approximation can be found in Ref. 10. Here, only the three final equations are presented along with the three variables to be solved, namely $\bar{c}_{\text{s}}$; the volume-averaged concentration flux $\bar{q}$; and the concentration at the surface of the AM particle, $c_{\text{s,surf}}$.

$$\frac{d\bar{c}_{\text{s}}}{dt} + 3 \frac{j_{\text{total}}}{r_{\text{p}}} = 0 \qquad [\text{E24}]$$

$$\frac{d}{dt}\bar{q} + 30 \frac{D_{\text{s}}}{r_{\text{p}}^2} \bar{q} + \frac{45}{2} \frac{j_{\text{total}}}{r_{\text{p}}^2} = 0 \qquad [\text{E25}]$$

$$35 \frac{D_{\text{s}}}{r_{\text{p}}}[c_{\text{s,surf}} - \bar{c}_{\text{s}}] - 8 D_{\text{s}} \bar{q} = -j_{\text{total}} \qquad [\text{E26}]$$

Notice that by combining E21 and E24, one gets:

$$\varepsilon_{\text{AM}}(-3) \frac{j_{\text{total}}}{r_{\text{p}}} = -\nabla \cdot \vec{n}_{\text{AM}-\text{AM}} - a_{\text{AM}-3} j_{\text{int},+} \qquad [\text{E27}]$$

Substitute $a_{\text{AM}-3}$, $\vec{n}_{\text{AM}-\text{AM}}$, and j_{total} gives:

$$\nabla \cdot \left(-\frac{\varepsilon_{\text{AM}}}{\tau_{\text{AM}}} D_s \vec{\nabla} \bar{c}_s \right) = \frac{3(1 - f_{\text{AM}-3})\varepsilon_{\text{AM}} j_{\text{AM}-\text{AM}}}{r_p} \qquad [\text{E28}]$$

where, $\frac{3(1 - f_{\text{AM}-3})\varepsilon_{\text{AM}}}{r_p}$ gives the specific interfacial area of AM in contact with other AM particles, so-called $a_{\text{AM}-\text{AM}}$ ($\text{m}^2_{\text{AM}-\text{AM}}/\text{m}^3_{\text{PA}}$).

The two boundary conditions are required for solving E28. The Li flux in the AM phase within the PA is equal to zero at the PA center by symmetry. At the PA surface, one makes the hypothesis of no charge transfer, hence the flux of lithium in the AM phase is zero

$$-\frac{\varepsilon_{\text{AM}}}{\tau_{\text{AM}}} D_s \vec{\nabla} \bar{c}_s \cdot \overrightarrow{r^*} = 0 \text{ at } r^* = R_{\text{PA}} \qquad [\text{BC14}]$$

$$-\frac{\varepsilon_{\text{AM}}}{\tau_{\text{AM}}} D_s \vec{\nabla} \bar{c}_s \cdot \overrightarrow{r^*} = 0 \text{ at } r^* = 0 \qquad [\text{BC15}]$$

At $t = 0$, the volume-average concentration of Li in all the AM particles is taken as:

$$\bar{c}_s(t = 0) = 0.38 * c_{s, \max} \qquad [\text{IC1}]$$

The initial concentration in the above equation is derived from PITT experiments on thin electrodes (see part I), which is a slow titration technique allowing the system to remain at a quasi-equilibrium state, given a potential window of 2.5–4.3 V vs Li$^+$/Li for the NMC electrodes.

Reaction rate.—The pore-wall flux $j_{\text{int},+}$ directly relates to the reaction rate occurring at the internal solid/liquid interface (i.e., between the AM and sub-pore domain within the PA). Thus, an equation is needed to simulate the kinetics of the reaction, which depends on the local concentrations and phase-potential difference at the interface. Butler-Volmer kinetic equation is used to this end:

$$j_{\text{int},+} = i_n^0 \left\{ \exp\left(\frac{(1-\beta)F}{RT}(\Phi_1 - \Phi_3 - U(c_{s,\text{surf}})) \right) \right.$$
$$\left. - \exp\left(-\frac{\beta F}{RT}(\Phi_1 - \Phi_3 - U(c_{s,\text{surf}})) \right) \right\} \qquad [\text{E29}]$$

where U represents the equilibrium potential of the AM that is a function of Li content; i_n^0 denotes the exchange current density.

For an insertion electrode involving the reaction $\text{Li}\Theta \leftrightarrow \text{Li}^+ + \Theta + \text{e}^-$, where Θ represents the solid lattice, the exchange current density depends on the lithium concentration in the electrolyte c_3 that fills in the sub-pores, the lithium concentration in the solid lattice $c_{s,\text{surf}}$ and the concentration of unoccupied sites in the lattice $c_{s, \max} - c_{s,\text{surf}}$ according to:

$$i_n^0 = F k_0 c_3^{1-\beta}(c_{s, \max} - c_{s,\text{surf}})^{1-\beta} c_{s,\text{surf}}^{\beta} \qquad [\text{E30}]$$

where k_0 is the rate constant of the electrochemical reaction. The exchange current density tends to zero as the solid concentration approaches either 0 or $c_{s, \max}$. Since the reaction-rate equation is algebraic, it requires no boundary condition.

The set of equations and corresponding boundary conditions used in the PApa model are summarised in Table I.

Compared with the Newman P2D model, the PApa model has three additional parameters, representing the fraction of particle surface in contact with electrolyte in sub-pores ($f_{\text{AM}-3}$), the PA radius (R_{PA}) and the volume fraction of the sub-pore domain among total porosity (ξ_3). The remaining parameters required for both models are listed in Table II for all the samples (measured at 25 °C).

Model validation against experimental results.—In this section, a model-based analysis of the rate capabilities of the four different industry-grade electrode designs with respect to their experimental results is detailed. Most of the parameters used in this section come from the first part of this series of papers, except for three additional parameters ($f_{\text{AM}-3}$, R_{PA}, ξ_3) of the PApa model introduced above.

Simulations for which local salt concentration reaches 3 mol l^{-1} anywhere across the cell sandwich are interrupted. In this situation, simulated values of the cell overpotential may still serve for comparison with experiments, whereas values of the delivered capacity are irrelevant and discarded.

It is worth noting that the model may not describe properly the Li plating/stripping mechanism at the "assumed" flat Li foil. During operation, the Li foil/electrolyte interface might not be very flat due to moss and/or non-uniform distributed current density, which can lead to a lower-than-expected Li$^+$ concentration in the vicinity of the foil. Consequently, at a high current density, the model can predict higher Li$^+$ concentration in the vicinity of the Li foil. Combined with the significant decrease of electrolyte properties at high concentration, the simulated discharge potential curve might show a fast drop and a much smaller EoD capacity than that observed in the experiments.

For some simulations, the cut-off voltage is set to 3.0 V to avoid convergence issues, as it causes only a minor difference in discharge capacity if it is set to 2.5 V instead.

Industry-grade-electrode validation.—Here, we focus on how discharge rate capability changes for different electrode designs to identify rate-limiting factors for each design. For this purpose, different electrolytes are used, resulting in different impacts on ionic transport. Using an electrolyte with low transport properties (LP40 1 M and 0.5 M) magnifies the discrepancy between electronic and ionic transport limitations. In contrast, ionic transport is improved with a high-performance electrolyte (LP30), so that its ionic transport limitations get closer to electronic ones. By changing the ratio between electronic and ionic transport, it can lead to either a more uniform reaction rate across the electrode (with LP30) or conversely a narrow reaction zone that moves across the PE as discharge proceeds (with LP40).[13] This is expected to provide more insights for understanding the interplay between electrode design and its performance.

Figure 2 summarizes the experimental rate capabilities of all industry-grade electrodes with three different electrolytes. Notably, all electrodes show very similar performance up to C/5, regardless of the type of electrolyte, which is also very close to that of the thin electrodes (see Fig. 3 in part I of this series of papers). This indicates that the limitations at low C-rates mainly come from the solid diffusion and charge transfer at particle scale, related to AM intrinsic properties rather than electrode design (PE scale).

As the discharge rate increases further (C/2 or more), the electrode performance starts to deviate from each other and from that of the thin electrode. This suggests a change in the electrode limitation, as the thickness increases, which is commonly explained by the contribution from porous-electrode effects, i.e., ionic/electronic transport. The Newman model should be able to capture this behavior, since the electrode tortuosity and electronic conductivity were carefully determined using appropriate experiments, as detailed in part I of this series of papers.

Also, it is noteworthy that a lower performance is observed experimentally for electrodes with a higher CB/binder content, despite a higher electronic conductivity. This result, albeit surprising at first sight, does not contradict other works in the literature.[14–17] One of the reasons is that a higher content of CB/binder leads to a higher electrode tortuosity factor, as the CBD tends to form clusters containing meso/nano-pores.[18,19] Another reason reported in Ref. 18 is that a decrease of the active surface area can also occur as AM particle surface is more covered by a higher amount of CBD, at the expense of the surface in contact with the liquid electrolyte. Moreover, despite its lower content of CB/binder, we observed a better dispersion of CBD in MX-01 than in MX-01b and MX-02b.[18]

Table I. Set of equations and corresponding boundary conditions used in PApa model.

Equations	Boundary conditions
$\Psi_2 \frac{\partial C_2}{\partial t} = -\nabla \cdot \vec{N}_{2,-} + A_{PA} j_{3,-}$	$\vec{N}_{2,-} \cdot \vec{n} = 0$ at $x = 0$ and $x = L_{el} + L_{sep}$
$\nabla \cdot \vec{I}_2 = A_{PA} F (j_{3,+} - j_{3,-})$	$\vec{I}_2 \cdot \vec{n} = 0$ at $x = L_{el} + L_{sep}$
	$\Phi_2 = 0$ at $x = L_{el} + L_{sep}$
$\nabla \cdot \vec{I}_1 = -A_{PA} F (j_{3,+} - j_{3,-})$	$\vec{I}_1 \cdot \vec{n} = I_{app}$ at $x = L_{el} + L_{sep}$
	$\vec{I}_1 \cdot \vec{n} = 0$ at $x = L_{sep}$
$\varepsilon_3 \frac{\partial c_3}{\partial t} = -\nabla \cdot \vec{n}_{3,-}$	$\vec{n}_{3,-} \cdot \vec{r^*} = 0$ at $r^* = 0$
	$c_3 = C_2$ at $r^* = R_{PA}$
$\nabla \cdot \vec{i}_3 = a_{AM-3} F j_{int,+}$	$\vec{i}_3 \cdot \vec{r^*} = 0$ at $r^* = 0$
	$\Phi_3 = \Phi_2$ at $r^* = R_{PA}$
$\frac{d\bar{c}_s}{dt} + 3 \frac{j_{total}}{r_p} = 0$	
$\frac{d}{dt} \bar{q} + 30 \frac{D_s}{r_p^2} \bar{q} + \frac{45}{2} \frac{j_{total}}{r_p^2} = 0$	
$35 \frac{D_s}{r_p} [c_{s,\,surf} - \bar{c}_s] - 8 D_s \bar{q} = -j_{total}$	
$\nabla \cdot \left(-\frac{\varepsilon_{AM}}{\tau_{AM}} D_s \vec{\nabla} \bar{c}_s \right) = \frac{3(1 - f_{AM-3}) \varepsilon_{AM} j_{AM-AM}}{r_p}$	$-\frac{\varepsilon_{AM}}{\tau_{AM}} D_s \vec{\nabla} \bar{c}_s \cdot \vec{r^*} = 0$ at $r^* = R_{PA}$
	$-\frac{\varepsilon_{AM}}{\tau_{AM}} D_s \vec{\nabla} \bar{c}_s \cdot \vec{r^*} = 0$ at $r^* = 0$

This promotes better short-range contacts[16,17,20] for electronic transport. It was experimentally demonstrated to be essential for electrode performance rather than long-range electronic conductivity, as it allows to have a more uniform distribution of reactions throughout the PE.

Regarding the simulations, Fig. 2 shows the corresponding results simulated with the baseline Newman P2D model. The model operates with the set of parameters determined in the first part of this series of papers without any fitting parameters. Unfortunately, there is a poor agreement between the model and the experimental results. The intrinsic active material properties were validated using rate capability data measured on a low-loading electrode (see part I). Both the solid diffusion coefficient and the reaction rate constant decrease as Li content approaches one. Nevertheless, the model tends to overestimate the performance in all cases, especially for moderate to high-rate discharge curves (*ca.* C/5 or larger). This is seen in Fig. 3a, in which the complete simulated and experimental discharge curves are compared for MX-01b in LP40 1 M. Similar to the low loading electrode, the polarizations of simulated curves are in agreement with the experimental curves at least at C-rates ⩽ C/2.

Although Malifarge et al.[21] demonstrated a good agreement between simulation and experimental results by measuring all the model parameters carefully in the case of graphite electrodes, the same approach on NMC positive electrodes does not seem to be as straightforward. Many literature works struggle to capture the correct discharge behavior at multiple C-rates using Newman model for the family of NMC materials.[1,2,14,22]

It is worth mentioning that in most of these literature works, an overestimation of predicted capacities is observed in the discharge simulations. The dominant performance-limiting factor is attributed to the ionic transport related to the liquid phase within the electrode porosity. Hence, they explain the performance overestimation by either an underestimation of the electrode microstructural parameters (e.g., τ_e) or an overestimation of the bulk electrolyte properties.

For instance, Higa et al.[22] proposed an approach, in which they carefully validated the intrinsic properties of their AM through the use of a "model" electrode, i.e., thin and highly porous, just like we do in this work. However, the authors had to assume a large electrode tortuosity factor ($\tau_e = 26$) to match the experimental data. Similarly, Tambio et al.[14] suggested increasing the tortuosity values for model validation due to the presence of micro/nano-porosities,

albeit the use of the geometric tortuosity factor, which is not appropriate to represent the tortuosity of the pore network within a PE.[23]

Even if the tortuosity factors in our work are not well determined by the symmetric cell method, the values are not expected to be too high as in Ref. 22.

Thus, attempts are made to adjust them for matching the experimental results and possibly verify assumptions on liquid-phase limitations. The case of MX-01b using LP30 1 M is first considered (Figs. 4a, 4b), in which MX-01b shows important capacity loss from rates above C/2 (*ca.* 1 mA cm^{-2}). An electrode tortuosity factor larger than 11 is needed to capture this behavior. Though, it does not affect the discharge at C/2. Figures 4c, 4d show simulation results of MX-02 with LP40 1 M, with an electrode tortuosity factor that is increased by a factor of 2 ($\tau_{e,\,fit} = 8$), which shows a better agreement with experimental data at the high discharge rates (1 C, 2 C). However, like MX-01b, this value does not resolve the difference between simulations and experimental results at lower discharge rates (C/5, C/2).

The analysis above has thus far suggested that the transport in liquid phase is likely not the solely limiting source of the electrode performance. Xu et al.[2] and Appiah et al.[1] tackled the issue differently, as they attributed the severe drop in capacity observed at high C-rate to the solid-state Li diffusion, which is a process occurring at the particle scale. However, using the Newman model, they had to exacerbate the limitation of this process through an empirical correlation of the solid-diffusion coefficient to either the electrode thickness or the C-rate to fit the experimental data. Even though both correlations allow for matching the experimental data, the underlying physics accounting for these dependencies is not clearly unravelled.

Back to the electrodes studied in this work, the worst performance is observed for electrodes with a higher content CB, so it is unlikely that the lack of limitations at the higher discharge rates of the simulations can be addressed by additional electronic resistances, which is frequently referred to as contact resistance between either particles or between porous electrodes and current collector. Furthermore, the change of electronic resistances mainly impacts the polarization of the discharge curves but has slight impacts upon the EoD capacity, unless there is a large distribution of contact resistances, with a fraction of poorly connected particles.
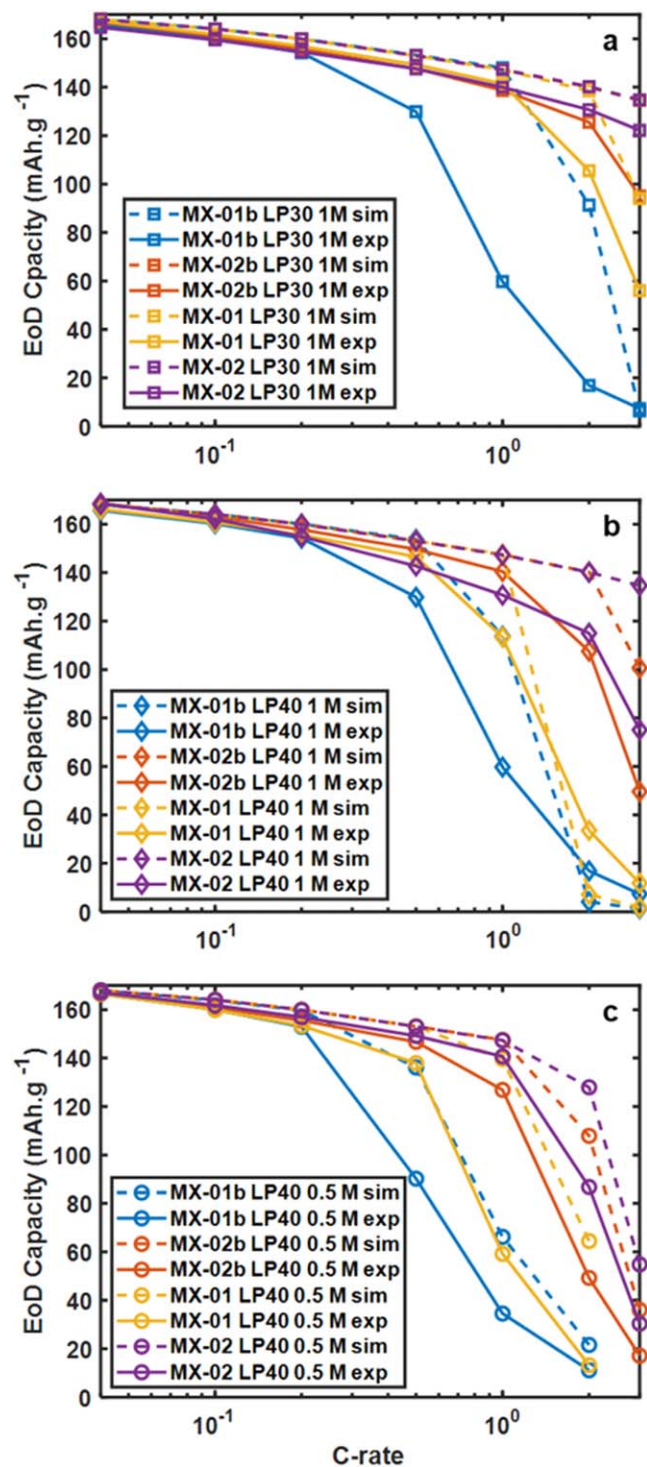
Figure 2. Validation on industry-graded electrodes with the baseline Newman P2D model. (a)–(c). Experimental (solid lines) and Simulation data (dashed lines) of the EoD Capacity in function of C-rate using LP30, LP40 1 M and LP40 0.5 M, respectively.
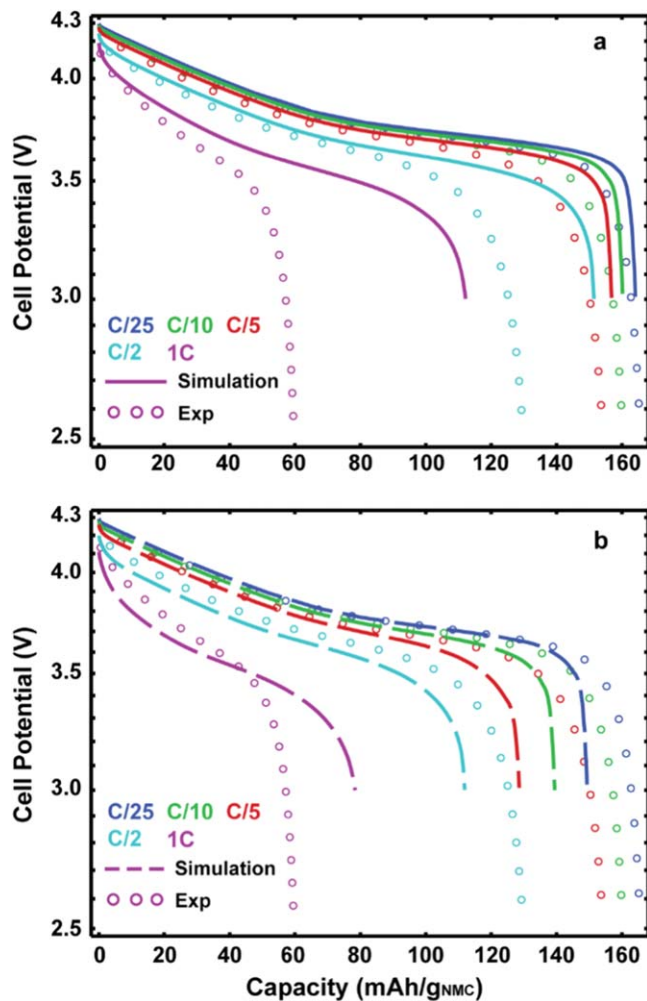

Figure 3. Influence of the particle size on the simulation results of MX-01b sample with LP40 1 M. (a). Simulation results using baseline Newman model with one particle size (2.35 μm diameter given by laser diffraction measurement). (b). Simulation results using baseline Newman model with a particle size of 10 μm diameter.

In this work, given that a good agreement between experimental and simulated rate-capability curves is obtained for thin electrodes up to very high C-rates (20 C corresponding to a current density of ~8 mA cm^{-2}), the parameters used for AM properties are expected to represent the AM behavior even in higher-loading electrodes correctly, as long as the assumptions at particle scale remain valid (e.g., isolated spherical particles).[13] Thus, the discrepancies indicate that the AM particle morphology in industry-grade electrodes might deviate from the "ideal" particle model used for the thin electrodes.

Fortunately, the analysis from tomographic data of the industry-grade electrodes can give more insights.[18] It shows a tendency of narrowing the gap between solid particles in the direction perpendicular to the current collector. In addition, a non-negligible extent of the inter-connectivity among AM particles is also quantified, which can reach up to 30% in average of the particle surface. Overall, the analysis implies a tendency of particle agglomeration (both AM and CBD). This deviates from the assumption of isolated AM particles in the baseline Newman model, in which the Li diffusion between adjacent AM particles, referred to as inter-particle diffusion, is not accounted for.[24]

Recently, the inter-particle diffusion was numerically demonstrated by Ferraro et al.[25] to occur between particles in contact. Assuming that the inter-particle diffusion is not affected by the particle-particle contact, then a group of particles in contact with each other would behave as a large single particle. The solid diffusion length increases, as it now relies on the size of the large particle agglomerate. This makes solid diffusion more critical. Moreover, the formation of particle clusters tends to reduce the active surface area, as particles are no longer fully exposed to the liquid phase as in the physical representation of Newman model. This causes fewer reaction sites dispersed over the particle surface,

resulting in longer diffusive pathways for "neutral" Li to move in order to occupy all the solid lattice during the discharge process.

If the solid diffusion process is the primary rate-limiting factor, a mere increase of the apparent particle radius, i.e., diffusion length, may reproduce the detrimental effects on electrode performance at high C-rates that are seen experimentally. Figure 3b shows that to match the high C-rate region, the increase of diffusion length will also overestimate the limitation at the low C-rate region and vice-versa. Therefore, an apparent particle size that empirically varies as a function of the C-rate would be required to fit the entire rate capability.

To conclude this part, the baseline Newman P2D model with a "micro" model that matches the AM behavior cannot match the discharge rate capabilities of the industry-grade electrodes. Different hypotheses are investigated to understand the root cause of the disagreement between simulations and experiments. Nevertheless, simply tuning an individual parameter to control either the liquid-phase transport (via τ_e) or the "micro" model behavior (via r_p) does not help reconcile simulations and experiments over the full range of C-rates. Even though Mistry et al. reported an outstanding agreement between experiments and model simulations using Newman P2D model by fitting the tortuosity factor as well as other microstructural properties (active surface area, electronic conductivity) for a batch of electrodes with different compositions and porosities and for a wide range of C-rates,[26] this is not the case in our study. Compared to Ref. 26, the electrodes studied in this work have a higher loading (15 & 25 mg cm^{-2} compared to 11.7 mg cm^{-2}). Later in our paper, we discuss the risk of agglomerate formation that increases with a high electrode loading and a high extent of calendering to achieve a high density. Thus, electrodes in Ref. 26 might suffer less from the

agglomerate formation, which is more aligned with the representation of the porous electrode in the Newman P2D model, i.e., having isolated solid particles. It might explain the disagreement between the results from Mistry et al.[26] and those from this paper. Here, the discrepancies between experiments and simulations may arise from extra limitation(s) for which the physics are not included in the baseline Newman model but can be relevant to electrodes in this study.

Given the high density of the industry-grade electrodes used in this work along with the analysis from tomographic data, the formation of particle agglomerates is likely to occur, which exacerbates the solid-diffusion limitations, as discussed above. However, we hypothesize that sub-pores can be located inside each agglomerate, making it a porous medium instead of a bulk nonporous agglomerate. In that case, the formation of agglomerates can also exacerbate the impacts from the ionic transport in the liquid phase. Since agglomerate formation decreases the available active surface area, which is also reduced by the CBD coverage, less reaction sites must support a higher pore-wall flux under the same current density. This accelerates the Li$^+$ depletion in the liquid phase in the vicinity of the reaction sites. Moreover, we assume that the pore network within the PA is formed by either the mesopores of the swollen CBD or the narrow gaps between solid particles due to the calendering process. Thus, the local highly-tortuous sub-pores are another source that would aggravate these local liquid-phase limitations.

Overall, the abovementioned combined effects (deterioration of solid diffusion, lowering of active surface area, and local Li$^+$ depletion in liquid phase) due to electrode calendering can be represented by a PA, in which solid particles are clustered together along with a low volume fraction of inter-connected sub-pores filled with electrolyte.
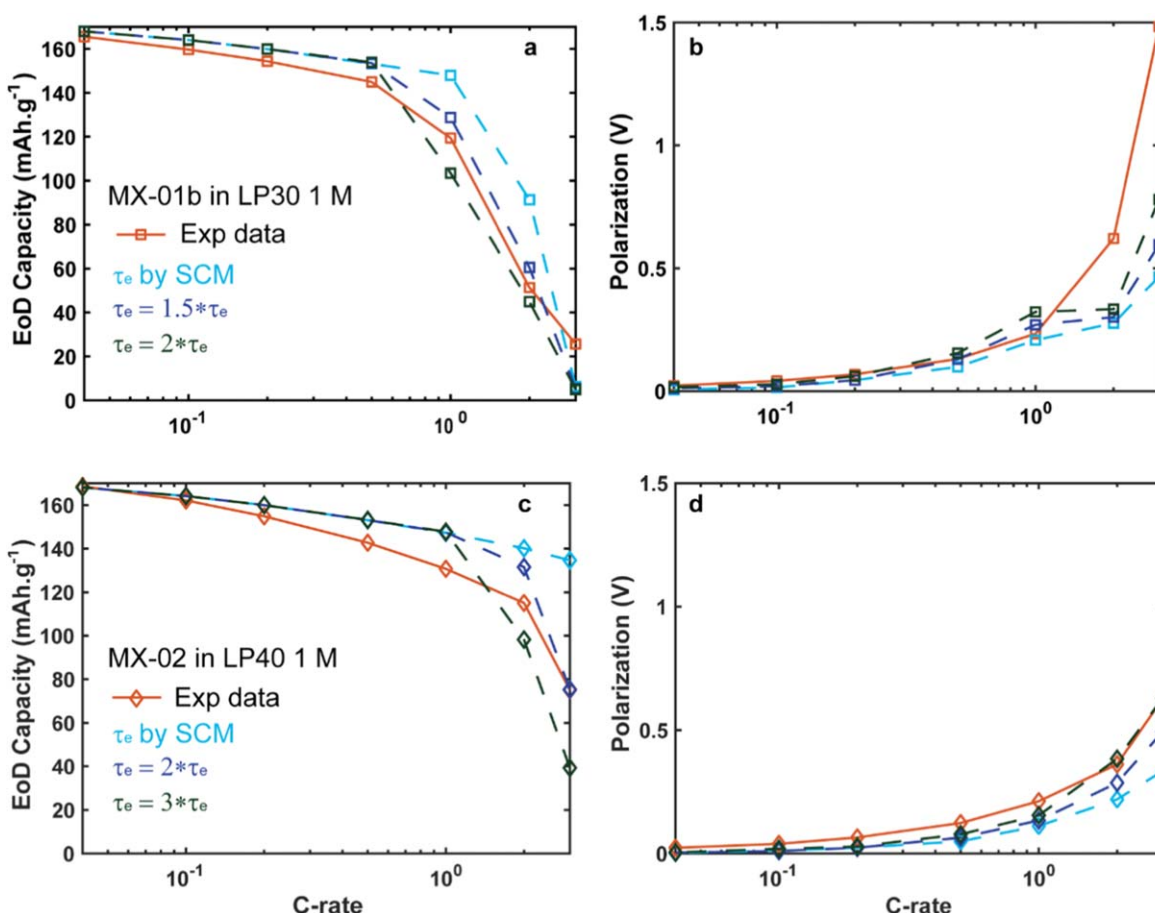

Figure 4. Study the effects of the electrode tortuosity factor on the simulation results. The electrode tortuosity factor was varied in two different cases to match the simulation results to the measurements. (a), (c). Comparison of EoD capacity between simulation and experiment for MX-01b and MX-02b, respectively. (b), (d). Comparison of polarization between simulation and experiment for MX-01b and MX-02b, respectively.

Table II. List of model parameters used for discharge process simulations at 25 °C.

Parameters		Values	
MX-01	**LP40 1 M**	**LP40 0.5 M**	**LP30 1 M**
d_{50}		4.7 μm	
Thickness, L_{el}	73.55 μm	72.13 μm	72.95 μm
Porosity, Ψ	0.24	0.24	0.25
McMullin number, $N_{M,e}$		17.47	
Electronic conductivity, σ_{eff}	0.11 S/m	0.11 S/m	0.11 S/m
%v AM, Ψ_{AM}	0.68	0.68	0.66
MX-02	**LP40 1 M**	**LP40 0.5 M**	**LP30 1 M**
d_{50}		4.7 μm	
Thickness, L_{el}	46.13 μm	46.40 μm	46.50 μm
Porosity, Ψ	0.28	0.25	0.25
McMullin number, $N_{M,e}$		17.56	
Electronic conductivity, σ_{eff}	0.16 S/m	0.16 S/m	0.16 S/m
%v AM, Ψ_{AM}	0.65	0.68	0.68
MX-01b	**LP40 1 M**	**LP40 0.5 M**	**LP30 1 M**
d_{50}		4.7 μm	
Thickness, L_{el}	74.35 μm	73.75 μm	74.45 μm
Porosity, Ψ	0.19	0.19	0.22
McMullin number, $N_{M,e}$		36.67	
Electronic conductivity, σ_{eff}	2.38 S/m	2.38 S/m	2.38 S/m
%v AM, Ψ_{AM}	0.70	0.67	0.67
MX-02b	**LP40 1 M**	**LP40 0.5 M**	**LP30 1 M**
d_{50}		4.7 μm	
Thickness, L_{el}	39.95 μm	39.95 μm	39.95 μm
Porosity, Ψ	0.16	0.18	0.17
McMullin number, $N_{M,e}$		24.35	
Electronic conductivity, σ_{eff}	3.07 S/m	3.07 S/m	3.07 S/m
%v AM, Ψ_{AM}	0.72	0.70	0.71

Figure 5 illustrates the geometric change from isolated-spherical particles to PA that is assumed to form on industry-grade electrodes due to calendering process. The CBD is assumed to be packed inside the PA and combines with AM particles to form the solid phase. Within a highly dense agglomerate, as shown in Fig. 5b, solid particles tend to share interfacial area between them (highlighted in green). Conversely, the particle surface area exposed to electrolyte (highlighted in red) is decreased. Although the particle/particle interface is considered electrochemical inactive, it allows for inter-particle diffusive flux of Li. Hence, inside a PA, two transport pathways co-exist, either solid diffusion through inter-connectivity between AM particles or ionic transport via electrolyte in sub-pores.

To numerically investigate this hypothetical scenario, an extension of Newman model, namely the PApa model, is developed and used to simulate the performance of the electrodes. In this model, the PA is assumed to be spherical, which has a radius, R_{PA}; whereas ξ_3
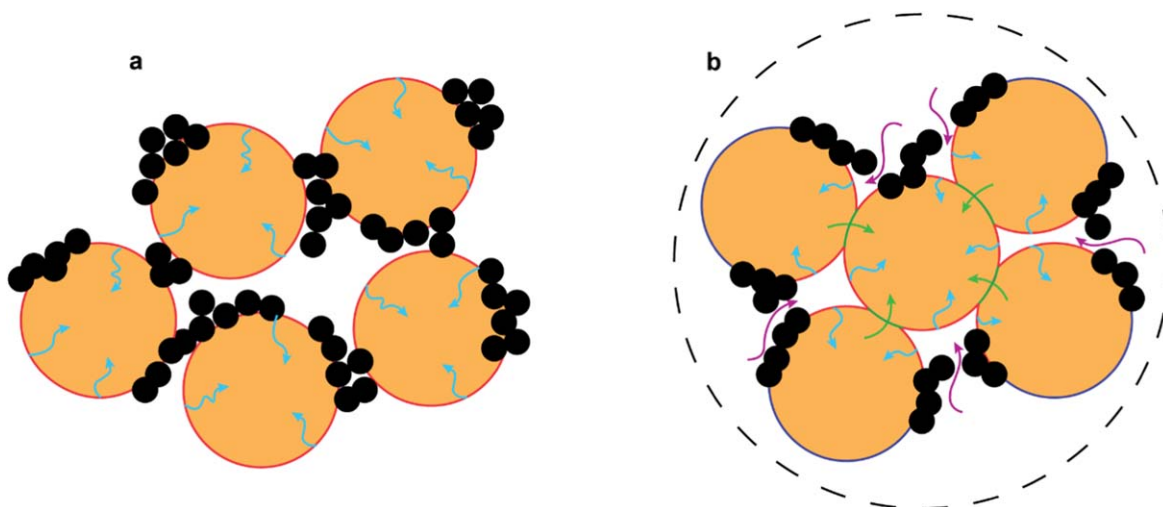

Figure 5. Our hypothesis of the formation of a PA. (a). Calendering process decreases the gap between solid particles (AM, CBD) leading to PA, in which a sub-pore domain contains some electrolyte. (b). Within the PA, there are two mechanisms of transport where a Li^+ can diffuse through liquid phase in the sub-pore domain or a bipolar $<Li^+,e^->$ can diffuse between secondary particles (interparticle solid diffusion). Ionic transport in sub-pore domain (magenta arrows), Inserted flux of Li^+ from electrolyte in sub-pores into individual AM particle (blue arrows), Inter-particle solid diffusion (green arrows). Active surface area is colored in red, Inter-connectivity between AM/AM is colored in green, Inactive surface area is colored in dark blue.
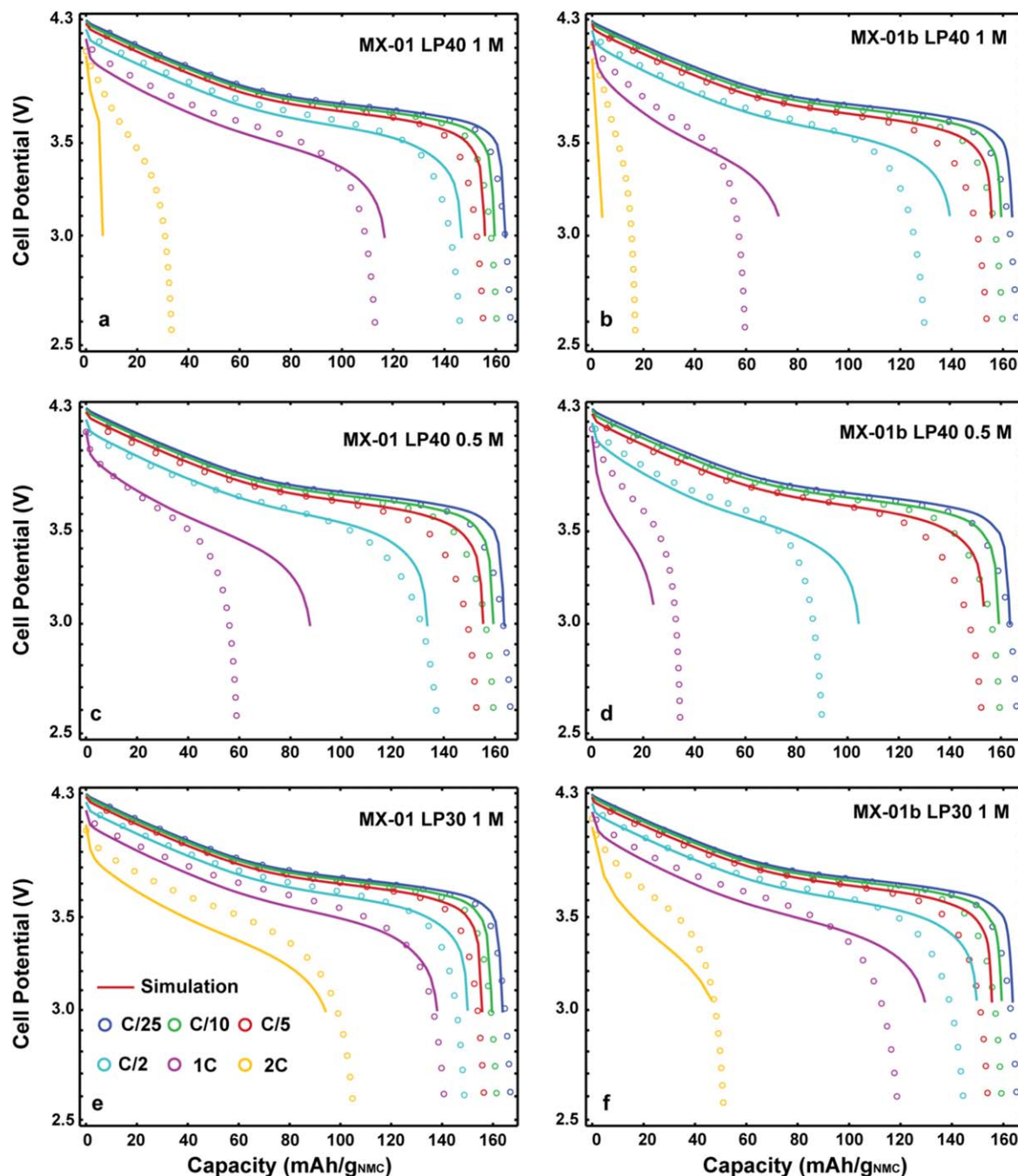
Figure 6. Validation of the PApa model on electrodes with loading of 25 mg cm^{-2}. (a), (c), (e). The discharge rate capabilities (C/25, C/10, C/5, C/2, 1C, 2C) using three different electrolytes (LP40 1M, LP40 0.5M, LP30 1M) are shown for MX-01. (b), (d), (f). The discharge rate capabilities (C/25, C/10, C/5, C/2, 1C, 2C) using three different electrolytes (LP40 1M, LP40 0.5M, LP30 1M) are shown for MX-01b.

represents the volume fraction of sub-pores among the total porosity. Since the AM particle surface is assumed to be in contact with either the electrolyte in the sub-pore domain or by other solid particles, a parameter representing the fraction of particle surface in contact with electrolyte in the sub-pores, f_{AM-3}, is also required.

Regarding the parametrization of the model, most of the parameters remain unchanged compared to the Newman model or can be estimated by empirical laws from literature. For macro-pore domain, it is decided that the electrode tortuosity factor value remains equal to that determined by the symmetric cell method, since the volume fraction of sub-pores is eventually shown to be very small in the simulations below. For the sub-pore domain, the tortuosity is assumed to follow the power-law fit ($\tau_e = 1.4\varepsilon^{-0.77}$)

from Usseglio et al.,[27] since this law already demonstrated a somewhat good agreement for electrode tortuosity at PE scale in our work (Fig. 6 of part I of this series of papers).

In the baseline Newman model, since the entire surface of a spherical particle is assumed to be exposed to the electrolyte, the fraction of particle surface in contact with other solid phases is zero. Here, characterization based on advanced X-ray tomography techniques provides insights. In Ref. 18, the microstructure of the three samples MX-01, MX-01b and MX-02b were investigated using X-ray holotomography, where the three phases: AM, CBD and electrolyte were completely resolved. Furthermore, the AM phase was separated into more than 500 individual particles, allowing for a statistical analysis of their inter-connectivity between different
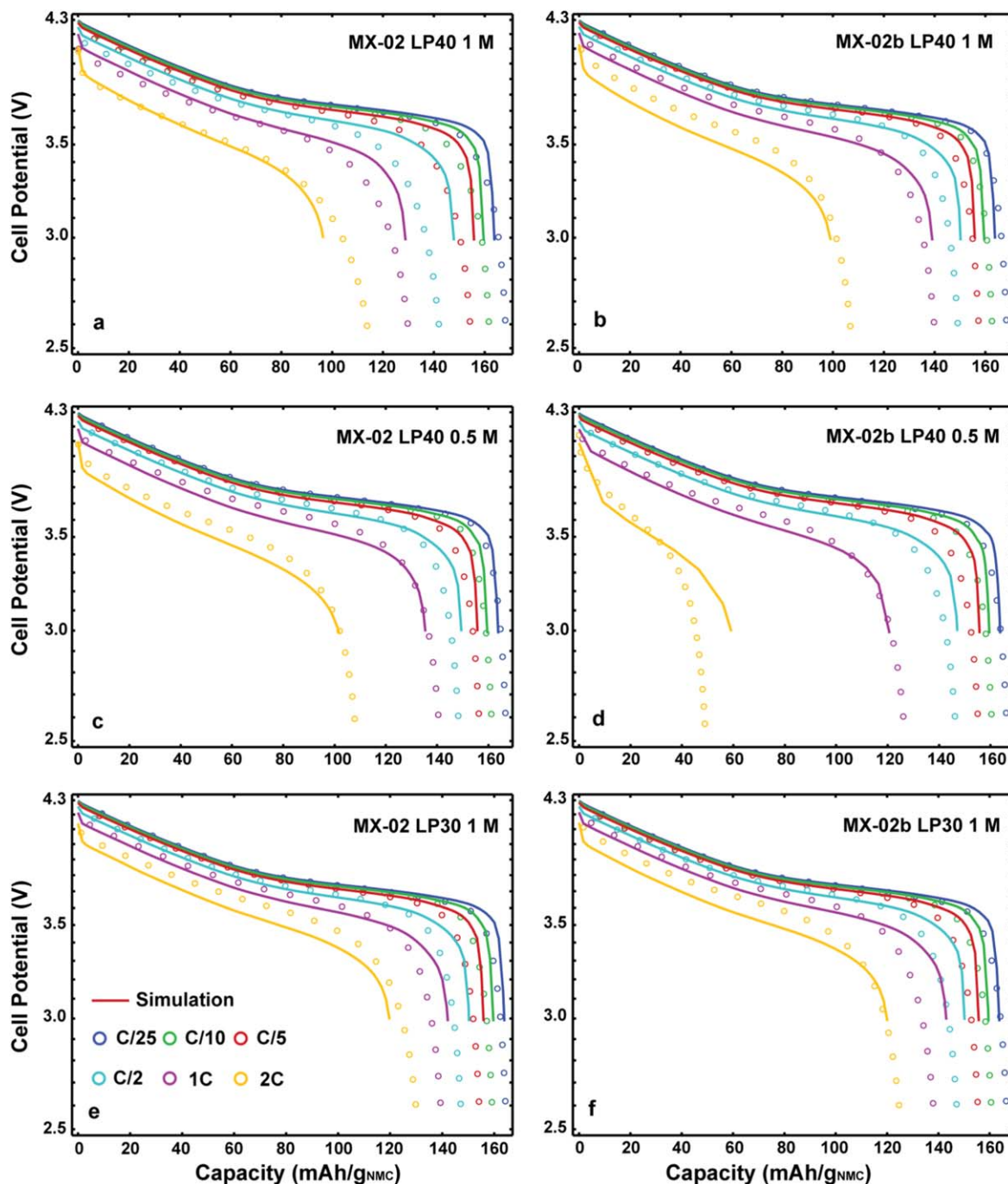
Figure 7. Validation of the PApa model on electrodes with loading of 15 mg cm^{-2}. (a), (c), (e). The discharge rate capabilities (C/25, C/10, C/5, C/2, 1C, 2C) using three different electrolytes (LP40 1 M, LP40 0.5 M, LP30 1 M) are shown for MX-02. (b), (d), (f). The discharge rate capabilities (C/25, C/10, C/5, C/2, 1C, 2C) using three different electrolytes (LP40 1 M, LP40 0.5 M, LP30 1 M) are shown for MX-02b.

phases. Therefore, f_{AM-3} of these samples in this work is taken as the average value of the inter-connectivity AM/electrolyte obtained from the statistical analysis, as shown in Fig. 5 of Ref. 18. It is worth noting that, in Ref. 18, we concluded that a higher amount of CBD and a higher density of the electrode decreases the AM/electrolyte interfacial area. Since we do not have the microstructural data for MX-02, the highest fraction of particle surface exposed to electrolyte compared to the other three is assumed for MX-02 based on the previous conclusion.

   Since f_{AM-3} is determined from Ref. 18 except for the MX-02 that is assumed, (R_{PA}, ξ_3) are the only two additional parameters, which are not determined from experiments. Therefore, they are

considered as fitting parameters to validate the experimental results. However, one must first verify whether they can be fitted independently. For that, they need to be independent of each other. Notably, these two parameters are connected through the characteristics time constant of the ionic transport within the sub-pore domain according to:

$$T_{\text{elyte, 3}} = \frac{R_{PA}^2}{D_{\text{eff, 3}}} = \frac{1.4 R_{PA}^2}{\varepsilon_3^{1.77} D} \qquad [E31]$$

given $\tau_3 = 1.4\varepsilon_3^{-0.77}$ as assumed earlier.

If the two parameters are correlated, the simulations remain unchanged as long as the group $\frac{\varepsilon_3^{1.77}}{R_{PA}^2}$ is kept constant, even though ε_3 and R_{PA} are modified. In other words, simulations with $R_{PA} = \gamma R_{PA,\,0}$, and $\varepsilon_3 = \gamma^{\frac{2}{1.77}}\varepsilon_{3,\,0}$ ($R_{PA,\,0}$, $\varepsilon_{3,\,0}$ are set) are identical whatever the value of γ. As a result, only the group can be fitted.

In Fig. S2a, one first investigates the case where the transport through the electrolyte in sub-pores dominates the inter-particle solid diffusion within the PA (e.g., highly porous agglomerate). In such case, since the PA radius is directly related to the solid diffusion, it has minor effects on the performance. This causes the difficulty to determine the PA radius independently from the sub-porosity.

Yet, in the case where the PA has negligible sub-porosity (ε_3 is small), inter-particle solid diffusion can substantially contribute to the mass transport at the PA scale along with the regular ionic transport via the electrolyte in sub-pores. As a result, the R_{PA} will have large impacts on the electrode performance, so that it can be decorrelated from the group in E31.

Hence, a sensitivity analysis of R_{PA} is performed for electrodes MX-01b and MX-02; corresponding to the two electrodes for which the inter-particle solid diffusion effects are the highest and lowest, respectively. In addition, only moderate to high C-rates are investigated since low C-rates are mainly limited by the solid diffusion in single particle and are not sensitive to inter-particle diffusion.

Figures S2b, S2c show the sensitivity of the R_{PA} on simulations while the value of the $\frac{\varepsilon_3^{1.77}}{R_{PA}^2}$ group remains invariant. The effects from R_{PA} are clearly observed on the simulated curves. A larger PA size deteriorates the electrode performance, as the inter-particle solid diffusion turns more critical.

Following the sensitivity analysis, one can, therefore, consider (R_{PA}, ξ_3,) as two separated parameters to be fitted unequivocally in the case where ξ_3 is considerably small. The tuning is manually performed by trial and error and assessing the qualitative agreement between experimental and simulations for each electrode in the three electrolyte compositions. These two parameters are adjusted for each electrode to achieve an overall good fit of all discharge C-rates and electrolyte compositions.

While baseline Newman model overestimates the rate performance for all the industry-grade electrodes studied here, as discussed above, the PApa model shows a very good agreement over a large range of C-rates for all four electrodes, even when different electrolytes are used (Figs. 6, 7). In most cases, the model simulations match well in terms of both polarization and EoD capacities. For higher loading electrodes (MX-01, MX-01b), as current densities get above 1 C (*ca.* 4 mA cm^{-2}), a mismatch between experimental and simulated data starts appearing for the LP40 electrolyte.

A possible reason for this mismatch is that the Li plating/stripping mechanism at the (assumed) flat Li foil is oversimplified in the model as discussed above. Higher concentration predicted by the model at the Li foil combined with low LP40 bulk properties at high concentration creates a large potential drop near the Li foil resulting in much less EoD capacity. Still, a good agreement is achieved for electrolyte LP30 with better transport properties. Also, this problem does not appear for lower loading electrodes (MX-02, MX-02b).

Figure 8a summarizes the two manually adjusted parameters required to validate the experimental results for the set of electrodes, whereas the fraction of particle surface exposed to electrolyte (from tomography analyses or assumed for MX-02) and the group $\frac{\varepsilon_3^{1.77}}{R_{PA}^2}$ are represented in Fig. 8b. A more sophisticated optimization process to better match the measurements can be applied for each electrolyte, but it can lead to different sets of (R_{PA}, ε_3). Thus, we decide to proceed with manually adjusted values to reach a good overall agreement for all the electrolytes with a unique set of input parameters for an electrode.
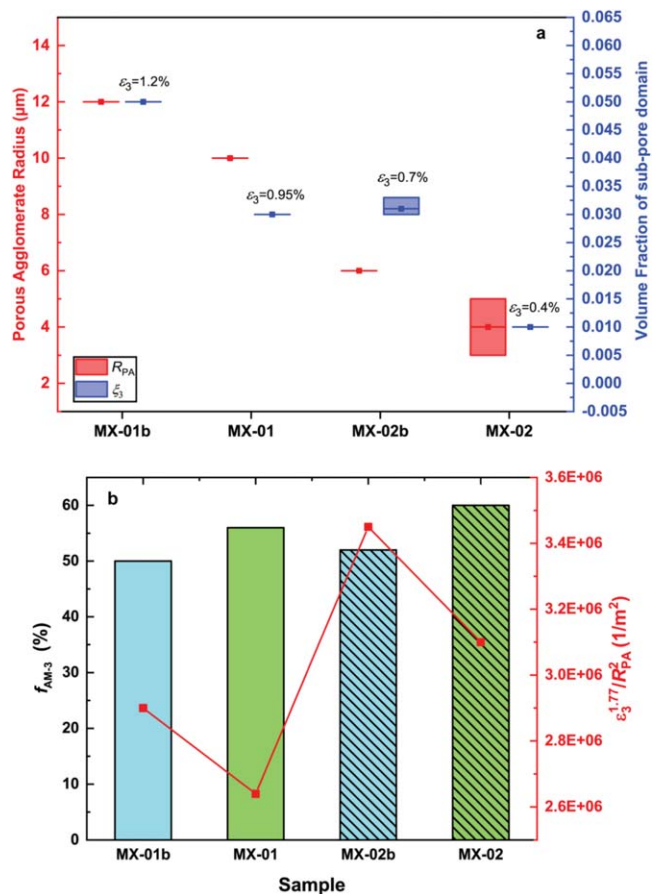

Figure 8. Summary of the two additional parameters used for PApa model. a. For each sample, the mean values of the two parameters (R_{PA}, ξ_3) are presented along with the shaded area representing the max/min values. b. The fraction of particle surface exposed to the electrolyte, f_{AM-3} obtained from tomographic data except for MX-02 that is assumed, and the invariant group, $\frac{\varepsilon_3^{1.77}}{R_{PA}^2}$ are also represented for each sample.

As mentioned above, the limitations from inter-particle diffusion are mainly related to the PA radius because the PA is highly dense ($\varepsilon_{AM} \rightarrow 1$). Thus, MX-01b is the most limited by the inter-particle diffusion among the electrodes. Moreover, the size of the PAs clearly shows a strong correlation with the electrode loading and density, i.e., electrodes with higher loading and density tend to have larger PAs due to the calendering process. By reducing the electrode loading by 40% (from 25 down to 15 mg cm^{-2}) for both compositions (either with 2.2% or 3.2%wt CB), the adjusted PA size decreases by about 50%, which can significantly benefit to the power performance. At iso loading, e.g., MX-02 and MX-02b, the electrode density shows a slight impact on the PA size.

Moreover, a higher fraction of pores that are sub-pores is observed for electrodes with a higher density and/or loading. Therefore, the transport limitations across the PE are exacerbated as the volume fraction of the macro-pore domain declines. The ionic transport in sub-pores can be better assessed via the group $\frac{\varepsilon_3^{1.77}}{R_{PA}^2}$, which directly relates to the characteristic time $T_{elyte,\,3}$. Interestingly, it is worth noting that no large variation is observed for the group $\frac{\varepsilon_3^{1.77}}{R_{PA}^2}$ from one electrode to another, which indicates that the extent of limitation from ionic transport in the sub-pore domain is tantamount for all electrodes. Besides, this also implies that among two transport pathways existing within the PA, the inter-particle diffusion relating to the PA radius shows a higher dependency on the electrode design.
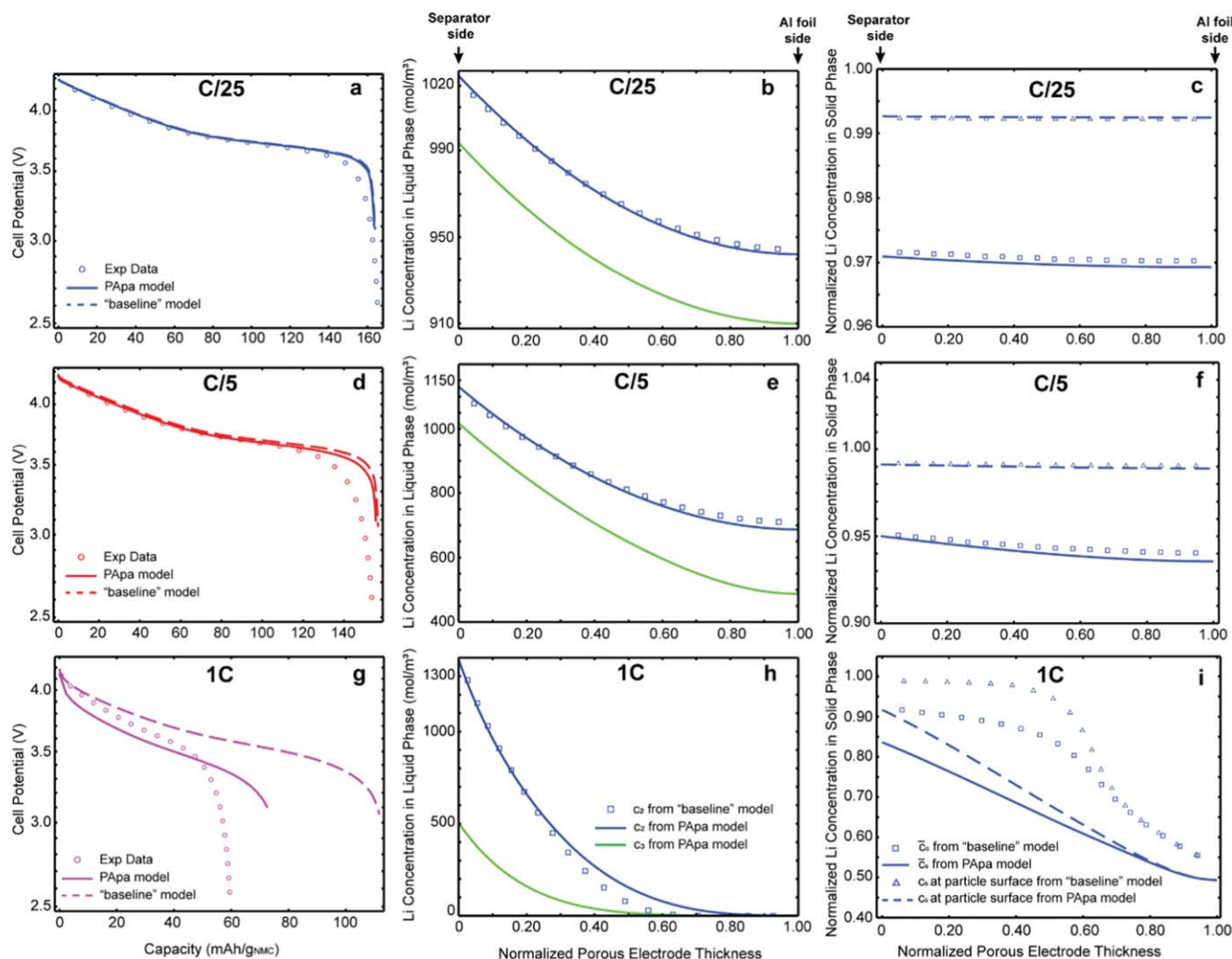
Figure 9. Comparison of concentration profiles in solid and liquid phases for MX-01b with LP40 1 M at EoD by baseline Newman and PApa models. (a), (d), (g). Comparison of the simulated discharge curves with the experimental data at C/25, C/5, 1C, respectively. (b), (e), (h). The concentration profile of Li$^+$ in liquid phase across the PE at C/25, C/5 and 1C, respectively. c, f, i. The local volume-average AM utilization and the local AM utilization at the particle surface across the PE at C/25, C/5 and 1C are represented, respectively.

MX-01b and MX-02b show larger PA size than their lower CB counterparts (MX-01 and MX-02), which undermines the inter-particle diffusion, albeit the PA is more porous (i.e., lower ionic limitations). This can be explained by their lower porosities needed to reach high density. Based on the Fig. 8a, the limitations by forming PAs in the calendering process can be decreased with higher porous and lower loading electrodes. Sample MX-02 provides the highest rate performance by virtue of its low loading and density, which result in less sub-pores and smaller particle agglomerates.

For an easier interpretation of the simulation results with the PApa model, the baseline Newman model simulations are used to compare low, moderate, and high C-rates for MX-01b. This enables more insights about the effects of the presence of PAs compared to the baseline situation.

Overall, a lower concentration in the sub-pore domain than in the macro-pore domain is observed at all C-rates, as expected. However, for low to moderate C-rates, the Li$^+$ concentration in sub-pores remains substantial (>0.4 mol l^{-1}), so that no complete Li$^+$ depletion occurs during the full discharge process (see Figs. 9b, 9e). Moreover, the concentration profile in the macro-pores of the PApa model does not show an important deviation from that in the liquid phase of the "baseline" model. This is because the sub-pore domain does not occupy a large volume fraction of the total porosity ($\xi_3 = 5\%$, which translates to a porosity for the PA of $\varepsilon_3 = 1.2\%$), so

the macro-pore domain behaves similarly to the total porosity under low-to-moderate current density (up to C/5 in Fig. 9e). Besides, the AM utilization (Figs. 9c, 9f) does not differ significantly between the two models, resulting in the same EoD capacity (Figs. 9a, 9d).

In contrast, at high C-rates, the concentration profile in the macro-pore domain starts to deviate more substantially from that of the baseline Newman model. The concentration in the sub-pore domain significantly drops even in the vicinity of the separator/PE boundary (Fig. 9h), resulting in local Li$^+$ depletion within this domain. Also, the AM utilization is significantly lower in the PApa model than in the Newman model (Fig. 9i), which results in a lower EoD capacity, thereby matching the experimental results.

In Fig. 10, the total Li flux defined in E23, the inter-particle diffusive flux and the charge-transfer flux are calculated per volume of PA by scaling with the AM particle surface, the coverage fraction by AM and electrolyte in sub-pores, respectively. This allows evaluating the main contribution of the inserted Li flux into the AM phase across the PA radius. At C/25, the ionic transport in sub-pores is not limited, so that the lithiation process is performed through electrochemical reactions. Consequently, the inter-particle diffusion flux is negligible. In contrast, at 1C, the inter-particle diffusion flux becomes important. A discrepancy between PA located at the separator side and the CC side is also highlighted upon the 1C discharge. The PA at the CC side is barely active, as the
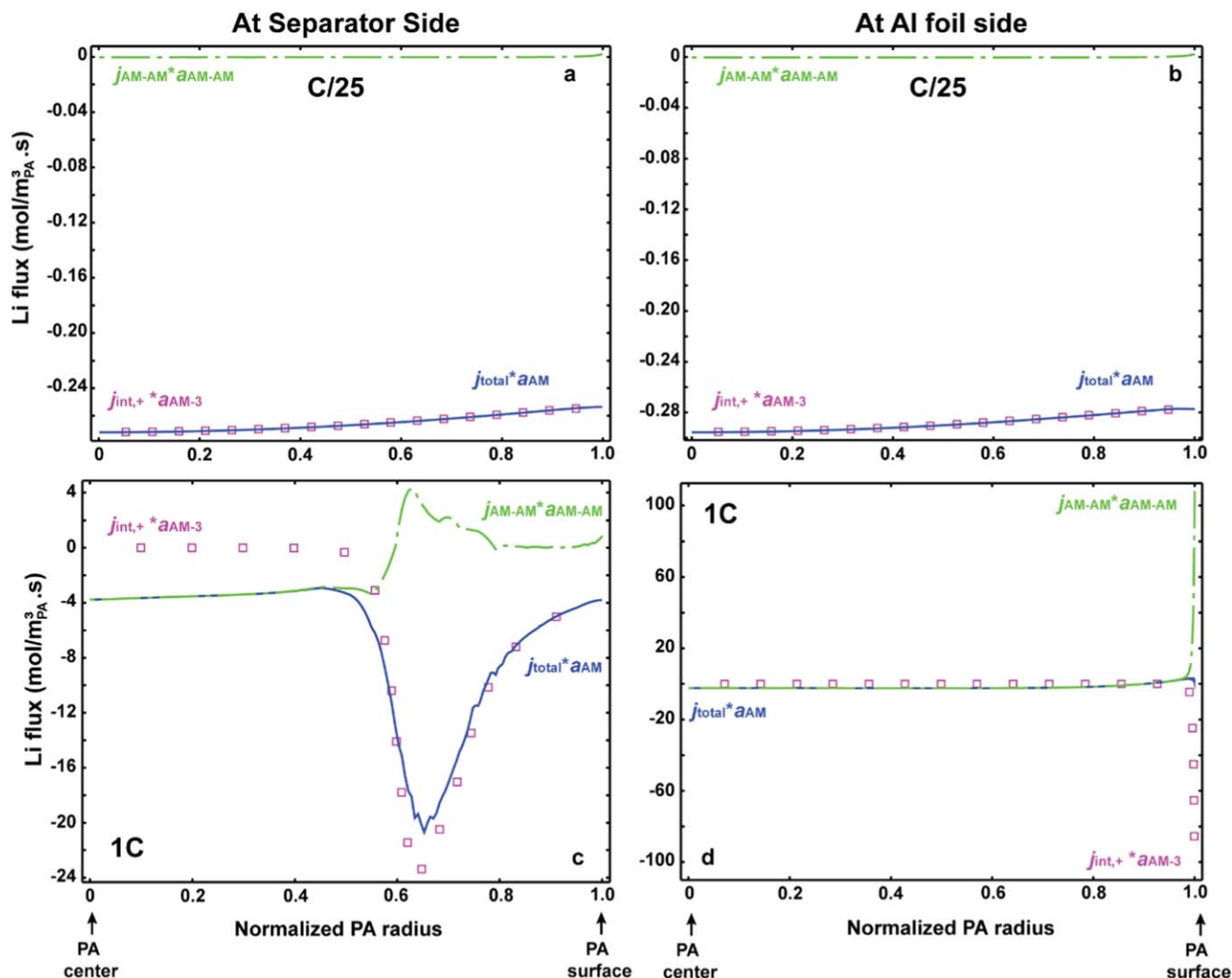
Figure 10. The Li flux flows within the PA at EoD. (a), (c). For PA located at separator side upon discharge at C/25 and 1C, respectively. (b), (d). For PA located at Al foil side upon discharge at C/25 and 1C, respectively.

flux entering the AM phase is minor compared to that of the PA at the separator side.

Interestingly, near the PA center, the inter-particle diffusive flux dominates, because a local depletion of Li^+ in the liquid phase prevents the charge-transfer to occur. In contrast, at the outer of the PA, the charge-transfer flux dominates the flux of Li^+ inserting into the AM particles, while there is an outward inter-particle diffusive flux leaving the particles at the outer to enter the particles at the inner (Fig. 10c). It is worth noting that the inter-particle diffusive flux is conserved over the PA volume, as any lithium leaving a particle of the agglomerate necessarily inserts into another particle. At 1C, at the CC, the reactions mostly occur at the vicinity of the pore mouth of the sub-pore domain (Fig. 10d). Also, a minor amount of Li then diffuses toward the PA center solely through the inter-particle diffusion process.

Model analysis.—One of the unique strengths of battery modeling is its ability to predict the distributions of current, potential, and concentrations across the full cell during cell operation. This often will provide information that is either difficult or impossible to determine experimentally and improve our understanding of the phenomena occurring inside the cells.

After the validation of experimental results, the model can be used for an in-depth analysis of the electrode performance, which allows resolving the electrode overpotential into separated

polarization sources and identifying performance limiting factors for each cell design (electrode design + electrolyte).

For this purpose, all the limitation sources are turned off sequentially. This means that some input parameter values are tuned so that limitations of corresponding physical phenomena are cancelled in the simulations. To this end, electrolyte conductivity, kinetic rate constant, and electrolyte/solid diffusion coefficient are set to high values. In addition, for electrolyte limitations shutdown, the lithium transference number and thermodynamic factor are set to one. It is worth noting that the electrolyte limitations in the sub-pore domain are combined with the inter-particle diffusion into a so-called porous agglomerate effect, since they are parallel transport pathways and cannot be completely decorrelated. The electrolyte limitations in the sub-pore domain are, therefore, separately investigated from those in the macro-pore domain.

Here, we investigate samples MX-01b and MX-02, which provide us with the worst and the best performance among the four electrode designs, respectively. Figure 11 shows three cases with low, moderate, and high current density for both electrodes. For both electrodes, at low C-rates, the performance is primarily limited by the solid diffusion within the secondary particles. This explains why the results simulated by the Newman baseline and PApa models are very similar at low currents. As the current density increases, different contributions from other sources are involved as limitations of the electrode performance. For MX-01b, albeit the PE limitations
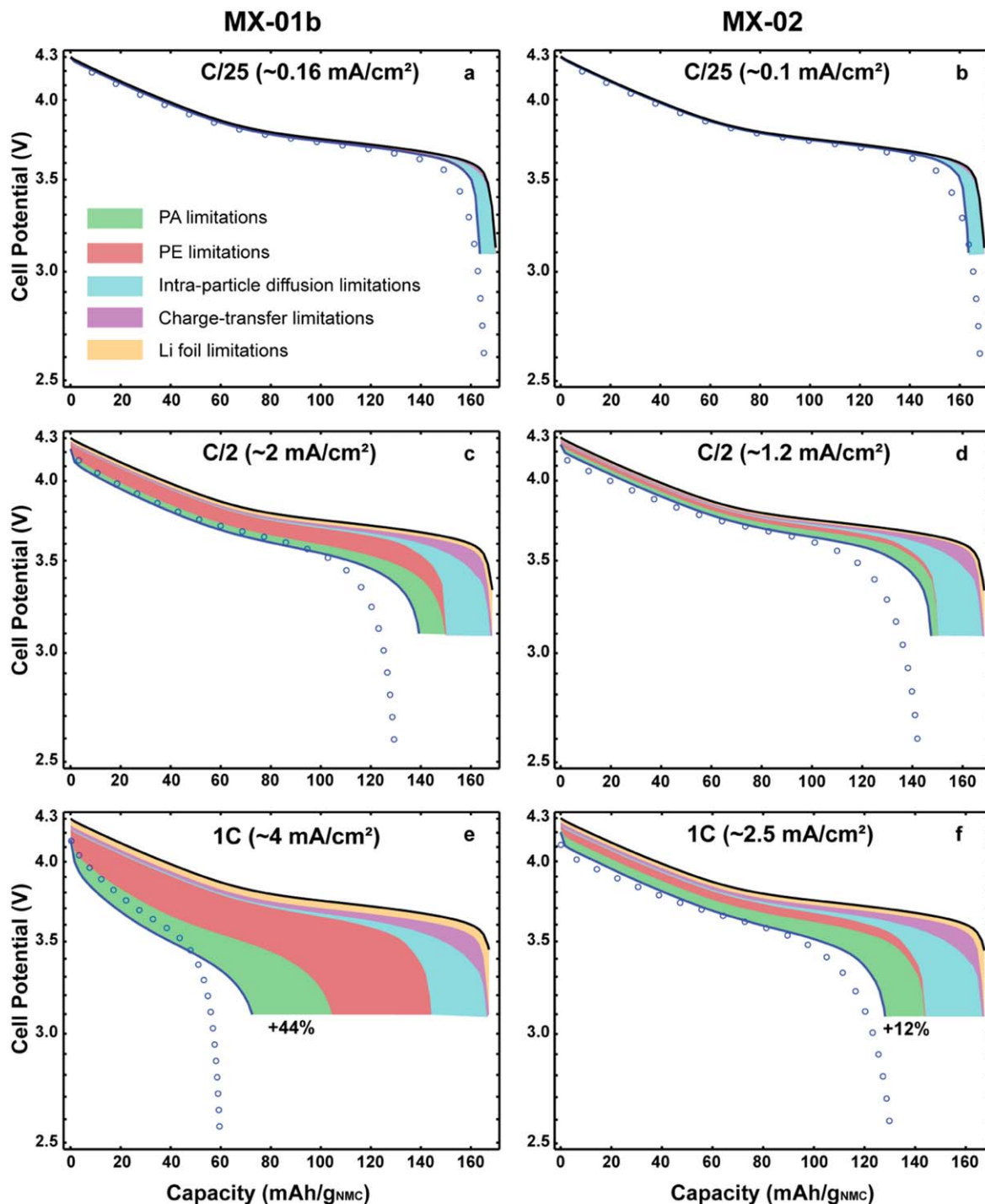
Figure 11. Decomposition of the potential curve. The potential curves along with experimental data (circles) at C/25, C/2 and 1C for MX-01b (a), (c), (e) and MX-02 (b), (d), (f) are resolved into different limitation sources. Starting from "as-is" simulations (blue line), porous agglomerate effects are first shutdown (light green), followed by porous electrode effects (light red), solid-phase diffusion intra-particles (cyan) and eventually the charge-transfer polarization (light purple). Lithium foil polarization (light orange) forms the last overpotential source up to the equilibrium potential represented as a solid black line.

still dominate as one moves to higher C-rates (1C, *ca.* 4 mA cm^{-2}), the effects from agglomeration become substantial. The rate capability of MX-01b can be considerably improved (up to 44% of EoD capacity at 1C) if we can avoid the negative effects stemming from agglomeration.

For MX-02, given its high porosity and lower loading, limitations from liquid phase are minor compared to other sources even at 1C. The limitations are mainly at the PA and the particle scales, as the intra-particle solid diffusion is the most critical followed by the PA

limitations. Without the presence of PAs, the rate capability of MX-02 can be improved up to 12% of EoD capacity at 1C.

Conclusions

Industry-grade electrodes with high loading and density are capable of storing large amounts of Li/energy, which is a requirement for battery packs in order to meet customer's expectations in terms of battery autonomy. However, the downside is that the power

capability of such electrodes is limited. In this work, the discharge performance limitations of these electrodes are investigated using physics-based models.

Regarding the experimental results, three different electrolytes are used to gain more insights on the effects of liquid-phase limitations upon discharge. Electrodes with higher amounts of CBD are found to exhibit a worse performance than those with a lower amount of CBD, despite a higher electronic conductivity. Tomographic data from our previous work suggested that the dispersion of CBD might play a crucial role to improve the rate performance.

First, the baseline Newman P2D model is used for validation of the experimental discharge rate capability of the four industry-grade electrodes at room temperature. Although this model on thin electrodes provides a strong agreement with the experimental data for the entire range of C-rates (up to 20C) (see the first part of this series of papers), its output only matches the experimental data at low C-rates, while it cannot represent the discharge behavior at higher C-rates for all the industry-grade electrodes. Different hypotheses from the literature are investigated, but none of these leads to adequate results.

Therefore, a modified macroscale battery model, referred to as the PApa model, is constructed, considering the effects of possible porous agglomerates originating from the severe calendering process undergone to densify the high-loading industry-grade electrodes. The proposed model has three additional parameters compared to baseline Newman P2D model. Since the X-ray tomography technique was used to quantify the fraction of particle surface exposed to the electrolyte, only two parameters (R_{PA}, ξ_3) were used as fitting parameters by which model output was tuned to match experimental results qualitatively for all electrode/electrolyte couples investigated in this work.

Compared to the Newman model, the PApa model showed a good agreement with the experimental results for all the industry-grade electrodes up to 4 mA cm^{-2} of current density. The values of fitting parameters (R_{PA}, ξ_3) are also qualitatively consistent with expectations. Higher-loading and higher-density electrodes result in a higher amount of pores that are sub-pores, and a larger apparent size of porous agglomerates. Both features exacerbate the limitations on the electrode performance.

For industry-grade electrodes used in this work, at low C-rates whenever the liquid-phase does not generate high limitations, solid diffusion within individual NMC secondary particles is the performance-limiting factor. As one moves to higher C-rates, the PA effects show up as a critical limitation source that deteriorates the rate performance of these electrodes. The model analysis suggests that a substantial gain in performance at high C-rates is expected if proper way rounds are figured to mitigate the agglomeration effects in these high-energy electrodes.

ORCID

Charles Delacourt https://orcid.org/0000-0001-5241-5441

References

1. W. A. Appiah, J. Park, S. Song, S. Byun, M. H. Ryou, and Y. M. Lee, *J. Power Sources*, **319**, 147 (2016).
2. M. Xu, B. Reichman, and X. Wang, *Energy*, **186**, 115864 (2019).
3. J. Newman and W. Tiedemann, *AIChE J.*, **21**, 25 (1975).
4. T. F. Fuller, M. Doyle, and J. Newman, *J. Electrochem. Soc.*, **141**, 982 (1994).
5. J. Newman, K. E. Thomas, H. Hafezi, and D. R. Wheeler, *J. Power Sources* (Elsevier, Amsterdam) 838 (2003).
6. S. Dargaville and T. W. Farrell, *J. Electrochem. Soc.*, **157**, A830 (2010).
7. S. Lueth, U. S. Sauter, and W. G. Bessler, *J. Electrochem. Soc.*, **163**, A210 (2016).
8. O. Birkholz and M. Kamlah, *Energy Technol.*, 2000910 (2021).
9. W. L. Bin Wu, *J. of The Electrochem. Soc.*, **163**, 3131 (2016).
10. V. R. Subramanian, V. D. Diwakar, and D. Tapriyal, *J. Electrochem. Soc.*, **152**, A2002 (2005).
11. R. Amin and Y.-M. Chiang, *J. Electrochem. Soc.*, **163**, A1512 (2016).
12. S. G. Stewart and J. Newman, *J. Electrochem. Soc.*, **155**, F13 (2007).
13. J. Newman and K. E. Thomas-Alyea, *Electrochemical Systems* (Wiley, USA) (2012).
14. S. J. Tambio, F. Cadiou, E. Maire, N. Besnard, M. Deschamps, and B. Lestriez, *J. Electrochem. Soc.*, **167**, 160509 (2020).
15. F. Cadiou, T. Douillard, N. Besnard, B. Lestriez, and E. Maire, *J. Electrochem. Soc.*, **167**, 100521 (2020).
16. S. L. Morelly, N. J. Alvarez, and M. H. Tang, *J. Power Sources*, **387**, 49 (2018).
17. R. Tang, Q. Yun, W. Lv, Y. B. He, C. You, F. Su, L. Ke, B. Li, F. Kang, and Q. H. Yang, *Carbon N. Y.*, **103**, 356 (2016).
18. T. Nguyen, J. Villanova, Z. Su, R. Tucoulou, B. Fleutot, B. Delobel, C. Delacourt, and A. Demortière, *Adv. Energy Mater.*, **11**, 2003529 (2021).
19. J. Landesfeind, M. Ebner, A. Eldiven, V. Wood, and H. A. Gasteiger, *J. Electrochem. Soc.*, **165**, A469 (2018).
20. H. Bockholt, M. Indrikova, A. Netz, F. Golks, and A. Kwade, *J. Power Sources*, **325**, 140 (2016).
21. S. Malifarge, B. Delobel, and C. Delacourt, *J. Electrochem. Soc.*, **165**, A1275 (2018).
22. K. Higa, S.-L. Wu, D. Y. Parkinson, Y. Fu, S. Ferreira, V. Battaglia, and V. Srinivasan, *J. Electrochem. Soc.*, **164**, 3473 (2017).
23. N. Epstein, *Chem. Eng. Sci.*, **44**, 777 (1989).
24. K. E. Thomas, R. M. Darling, and J. Newman, *Advances in Lithium-ion Batteries*, ed. W. Van Schalkwijk and B. Scrosati (Kluwer Academic, USA) (2002).
25. M. E. Ferraro, B. L. Trembacki, V. E. Brunini, D. R. Noble, and S. A. Roberts, *J. Electrochem. Soc.*, **167**, 013543 (2020).
26. A. Mistry, S. Trask, A. Dunlop, G. Jeka, B. Polzin, P. P. Mukherjee, and V. Srinivasan, *J. Electrochem. Soc.*, **168**, 070536 (2021).
27. F. L. E. Usseglio-Viretta et al., *J. Electrochem. Soc.*, **165**, A3403 (2018).